AGU ADVANCING EARTH AND SPACE SCIENCE

Earth and Space Science

RESEARCH ARTICLE
10.1029/2021EA002104

Visible to Mid-Infrared Optical Constants of Orthopyroxenes

Melinda J. Rucks[1], Cheng Ye[2,3], Elizabeth C. Sklute[4], Jessica A. Arnold[5], Nicholas J. DiFrancesco[6], and Timothy D. Glotch[2]

[1]Princeton University, Princeton, NJ, USA, [2]Stony Brook University, Stony Brook, NY, USA, [3]Northern Arizona University, Flagstaff, AZ, USA, [4]Planetary Science Institute, Tucson, AZ, USA, [5]Army Research Lab, Adelphi, MD, USA, [6]SUNY Oswego, Oswego, NY, USA

Key Points:

- Optical constants are necessary inputs into remote sensing models that quantitatively determine modal mineralogies on planetary surfaces
- Many optical constants available are end member compositon only
- Here we calculate the optical constants for two compositions of orthopyroxene, common minerals observed on planetary surfaces, in the visible/near infrared and mid to far infrared

Supporting Information:

Supporting Information may be found in the online version of this article.

Correspondence to:

M. J. Rucks,
mrucks@princeton.edu

Citation:

Rucks, M. J., Ye, C., Sklute, E. C., Arnold, J. A., DiFrancesco, N. J., & Glotch, T. D. (2022). Visible to Mid-infrared optical constants of orthopyroxenes. *Earth and Space Science*, *9*, e2021EA002104. https://doi.org/10.1029/2021EA002104

Received 1 NOV 2021
Accepted 23 FEB 2022

Author Contributions:

Conceptualization: Timothy D. Glotch
Data curation: Melinda J. Rucks
Formal analysis: Melinda J. Rucks
Funding acquisition: Timothy D. Glotch
Investigation: Melinda J. Rucks, Elizabeth C. Sklute, Nicholas J. DiFrancesco
Methodology: Melinda J. Rucks, Cheng Ye, Elizabeth C. Sklute, Jessica A. Arnold, Timothy D. Glotch
Project Administration: Timothy D. Glotch

Abstract Radiative transfer models of remotely acquired infrared spectra result in quantitative identification of minerals on planetary surfaces. Optical constants, or the real (n) and imaginary (k) indices of refraction are necessary inputs in such models. Pyroxenes are ubiquitous on the surfaces of terrestrial bodies within our solar system and can be readily used as thermo-barometers to interpret magmatic histories. However, optical constants for intermediate pyroxene compositions are undetermined. Here, we have determined the optical constants of two natural orthopyroxenes both in the visible/near-infrared (VNIR) and mid-infrared (MIR) regions. VNIR reflectance spectra were measured using powdered samples and modeled using a combination of Hapke theory and Kramers-Kronig analysis. MIR reflectance spectra were measured on oriented single crystal samples with non-normal incidence and modeled using Lorentz-Lorenz dispersion theory. The optical constants derived here are available to the scientific community at https://doi.org/10.5281/zenodo.4758045 to be used in the interpretation of remote sensing data.

1. Introduction

Pyroxenes are among the most abundant rock-forming minerals found in the Solar System and have been detected on the Moon, Mars, rocky asteroids, and interplanetary dust particles (IDPs). The structure of pyroxenes can be broadly subdivided into orthopyroxenes (OPX) and clinopyroxenes (CPX), having orthorhombic and monoclinic symmetry, respectively. Both structure types, consists of alternating tetrahedral and octahedral layers along the c-axis (Cameron & Papike, 1981). The octahedral layer includes two metal cation sites, M1 and M2. The M1 site allows for normal octahedral coordination, predominantly occupied by Mg^{2+} and Fe^{2+}, and the M2 site is in slightly disordered octahedral coordination, accommodating large cations, such as Ca^{2+} (Morimoto et al., 1988). End members are: enstatite (En: MgSiO3), ferrosilite (Fs: FeSiO3), and wollastonite (Wo: CaSiO3). OPX are Mg-Fe rich, containing only up to 5% of wollastonite component. Monoclinic pyroxenes have higher contents of Ca. The distribution of iron between the M1 and M2 sites is a function of composition, temperature, pressure, and cooling history (Anovitz et al., 1988; Klima et al., 2007, 2008; Molina & Zanazzi, 1991; Saxena et al., 1974; Virgo & Hafner, 1970). Thus, the quantitative characterization of pyroxene mineralogy of planetary surfaces is indicative of magmatic evolution and cooling conditions of the source rock (Klima et al., 2008; Lindsley, 1983).

The determination of pyroxene composition through electronic and vibrational spectroscopy, particularly in the near- to MIR (mid-infrared) range with applications to remote sensing, has been the subject of several studies (Adams, 1974; Cloutis & Gaffey, 1991a, 1991b; Hamilton, 2000; Klima et al., 2007, 2008; Klima, Dyar, et al., 2011; Sunshine et al., 1990; Sunshine & Pieters, 1993). Observed IR spectral features result from both electronic and vibrational phenomena. The absorption, transmission, or reflection at a particular wavelength of light is specific to the ion and its bonding environment within a crystal lattice. Absorption in the visible to near-infrared (VNIR; ~0.4–2.5 μm) is the result of electronic transitions involving Fe, whereas features in the MIR(~2.5–50 μm) are due to crystal lattice vibrations.

In the VNIR, pyroxenes exhibit two major absorption bands near 0.9 μm (Band 1) and 1.9 μm (Band 2) resulting from Fe^{2+} crystal field transitions (Adams, 1974; Rossman, 1980). The positions and areas of the absorption bands have been correlated to composition and preferential site occupancy into the pyroxene structure, where the M1 site contributes to Band 1 and the M2 site can contribute to both Band 1 and 2. As such, these features are useful diagnostic tools to infer pyroxene composition. For pyroxenes containing <10% of wollastonite component, the central positions of Bands 1 and 2 can be linearly correlated to Fe^{2+} content as both bands shift toward longer wavelengths occur as a function of increasing Fe^{2+} content (Burns, 1965; Cloutis & Gaffey, 1991b).

Resources: Timothy D. Glotch
Software: Elizabeth C. Sklute
Supervision: Timothy D. Glotch
Validation: Melinda J. Rucks
Visualization: Melinda J. Rucks
Writing – original draft: Melinda J. Rucks
Writing – review & editing: Melinda J. Rucks, Cheng Ye, Elizabeth C. Sklute, Jessica A. Arnold, Nicholas J. DiFrancesco, Timothy D. Glotch

Similar shifts are observed with increasing Ca^{2+} content, where more drastic changes in the band 2 positions are seen for pyroxenes up to Ca^{2+} saturation at the M2 site. Due to the primary occupancy of the M2 site by Ca^{2+}, the Fe^{2+} spectral trend can be masked for Ca-rich pyroxenes (>50% Wo; Klima, Dyar, et al., 2011). Several other cations affect the spectral signature of pyroxenes as well, including a shift of both major bands to shorter wavelengths with increasing aluminum content, for example, in terms of spectral shift, every 1 wt.% of Al^{3+} is approximately equivalent to a 5% decrease in Fe^{2+} (Cloutis & Gaffey, 1991b). Thus, VNIR spectroscopy alone is insufficient to quantitatively estimate pyroxene composition.

The MIR yields detailed structural information as the location and number of spectral features are directly related to the vibrational modes of repeating units within a crystal structure. In particular, the MIR is sensitive to Si-O vibrational modes (Arnold et al., 2014; Hamilton, 2000; Salisbury, 1972). This makes the MIR spectral range ideal for remote sensing applications Analysis in this region yields information about the whole composition of the material directly related to its structure. In the case of pyroxenes, spectral features are the result of Si-O vibrational modes as well as M-O vibrational modes (Farmer, 1974; Jäger et al., 1998). Analysis of MIR spectral data is complicated, however, by multiple scattering effects that result in reductions in fundamental band strength, the appearance of transparency features, and nonlinear spectral mixing when particle sizes are similar to or smaller than the wavelength of light (e.g., Salisbury & Wald, 1992).

Radiative transfer (RT) models are commonly used to analyze remotely sensed data to quantitatively determine the mineral compositions of planetary surfaces at wavelength ranges and grain sizes where linear mixing cannot be assumed. By directly modeling light interacting with the surface as a function of particle size, composition, roughness, incidence, and emission angles, etc., quantitative abundances can be estimated, provided that the necessary input parameters are known. Such models include those by Hapke (1981, 1996, 2012), Lumme and Bowell (1981), Mishchenko et al. (1999), and Shkuratov et al. (1999). An essential input into these light scattering models is the complex index of refraction, $\tilde{n} = n + ik$, where n and k are the real and imaginary indices of refraction, also known as optical constants. The optical constants are fundamental bulk properties of any given mineral that depend on both composition and crystal structure.

The two models most often used in planetary remote sensing applications are those of Hapke (1981, 1996, 2012) and Shkuratov et al. (1999). In Hapke's theory, n and k are used to calculate both the single scattering albedo ($\omega_{0\nu}$) and the Ambartsumian-Chandrasekhar H-function, (H(x)), which are used to solve the radiative transfer equation to model reflectance (Chandrasekhar, 1960; Hapke, 1981, 1996, 2012). In this case, while reflectance is not linear with composition under many conditions (specifically in the VNIR), single scattering albedo does vary linearly with percentage in an intimate mixture (either mol% or vol%, depending on several modeling factors), and thus the bulk single scattering albedo derived from a remote reflectance measurement can be used to extract quantitative abundance information. Skhuratov's model describes the reflectance (A) as a function of the four parameters $n, k, S,$ *and* q, where n and k are the optical constants, S is the scattering path-length, and q is the particle packing density (Shkuratov et al., 1999). As noted by Sklute et al. (2015), k in Shkuratov's approximation of radiative transfer are dependent upon the path length light travels in the material. Therefore, the value calculated with this model, while potentially useful, is not strictly representative of the actual k of the material in question. Thus, while this model is useful in modeling surface composition if n and k are already known, it is not appropriate for the derivation of optical constants through inverse modeling. In either case, the successful use of RT models to make quantitative estimates of regolith surface composition and physical properties hinges on the availability of optical constants for a range of major rock forming minerals.

The values of n and k values have been determined for only a few planetary relevant rock-forming minerals and are often only derived for a few compositions at limited wavelengths; such minerals include quartz (Spitzer & Kleinman, 1961; Wenrich & Christensen, 1996), gypsum (Aronson et al., 1983), orthoclase (Aronson, 1986), calcite (Lane, 1999; Roush, 2021), magnesite (Roush, 2021), dolomite (Roush, 2021), olivine (Dyar et al., 2009; Lucey, 1998; Suto et al., 2002), orthopyroxene (Jäger et al., 1998), clinopyroxene (Arnold et al., 2014), labradorite (Ye et al., 2019), palagonite (Roush et al., 1991), phyllosilicates (Glotch et al., 2007), and iron oxides (Glotch & Rossman, 2009). The optical constants of OPX have previously been determined in both the VNIR (Denevi et al., 2007; Lucey, 1998; Roush et al., 1991; Trang et al., 2013) and MIR spectral ranges (Jäger et al., 1998). Most of these studies report “bulk”, or orientation-averaged, effective optical constants, using powdered samples. Only a few report orientation-dependent MIR single-crystal optical constants for enstatite single crystal have been reported for enstatite (Mg# = 0.92–0.96) at different temperatures (Zeidler et al., 2015) and at ambient

Table 1
Existing Optical Data for Orthopyroxenes

Publication	Mg # range	Number of samples	Spectral range (μm)	Comments
Roush et al., 1991	0.86	1	5.0–25.0	*k* only; powder and crystal slab; un-oriented
Jäger et al., 1998	0.97	1	2.0–100.0	*n* and *k*; oriented single crystal
Lucey, 1998	0.57–0.92	8	0.3–2.6	*k* only; powder
Denevi et al., 2007	0.08–0.92	19	0.3–2.6	*k* only; powder
Trang et al., 2013	0–0.98	24	0.3–2.6	*k* only; powder
Zeidler et al., 2015	0.92	1	5.0–60.0	*n* and *k*; oriented single crystal
This study	0.77–0.86	2	2.5–40	*n* and *k*; oriented single crystal

temperature (Jäger et al., 1998). Mg# is equal to ($Mg/(Mg + Fe^{2+})$). Yet, oriented single crystal values are particularly valuable, as they provide all complex indices of refraction for a specific mineral composition at a given wavelength.

A summary of all pyroxene compositions for which optical data has been derived is shown in Table 1. In this work, the values of *n* and *k* have been determined using dispersion analysis for two unique OPX compositions in the range of 250–4,000 cm^{-1} (2.5–40 μm) following the methods outlined by Glotch et al. (2006, 2007) and Arnold et al. (2014). In addition, the bulk VNIR optical constants for these same samples were calculated here following the procedure outlined in Sklute et al. (2015, 2021) and Ye et al. (2021). Previous works deriving optical constants of OPX are summarized in Table 1.

2. VNIR and MIR Characterization of Pyroxenes in the Solar System

2.1. Moon

The Clementine mission enabled multispectral VNIR global mapping of lunar surface composition, highlighting the heterogeneity of lunar regolith both laterally and with depth. Pyroxene was found to be the major component in mafic rocks, predominantly present in mare basalts and only as a minor component of the Mg-suite and ferroan anorthosite (FAN) rocks of the lunar highlands (Tompkins & Pieters, 1999). Cahill and Lucey (2007) and Cahill et al. (2009) used radiative transfer models of Clementine UVVIS and NIR data to study the global distribution of major minerals as a function of latitude, longitude, and crustal depth, finding exposures containing low-Ca pyroxene (LCP), at the South Pole-Aitken basin (SPA) and in a few crater peaks within the Procellarum KREEP (Potassium, Rare Earth Elements, and Phosphorus) Terrane (PKT). Expanding on these results (Klima, Pieters, et al., 2011), used the Modified Gaussian Model (MGM) to deconvolve NIR spectral data from the Chandrayaan-1 Moon Mineralogy Mapper (M^3) to constrain the distribution and composition of LCP with respect to candidate Mg-suite intrusions. LCPs were found to be regionally constrained to craters within SPA and to the north and south of Mare Frigoris in the northern hemisphere near side. Approximately half of the pyroxenes modeled are compositionally comparable to those found in conjunction with Fe-enriched (Mg # 55–75) FAN suite rocks.

The Diviner Lunar Radiometer Experiment aboard the Lunar Reconnaissance Orbiter (LRO) introduced complementary MIR multi-spectral data to the Clementine and M^3 VNIR spectral measurements, enabling the detection of iron-poor lithologies where mafic minerals are present. Diviner includes 3 channels devoted to mineral detection that have narrow passbands centered around 8 μm (Greenhagen et al., 2010). This region exhibits the emissivity maximum, or Christiansen feature (CF), associated with degree of SiO_2 polymerization where the CF positions shift to shorter wavelengths with an increase in SiO_2 polymerization (Conel, 1969; Greenhagen et al., 2010; Nash et al., 1993; Salisbury & Walter, 1989). Analysis of the CF region, as well as other major MIR features, including the Reststrahlen bands, is well suited to identify and distinguish Fe-poor lithologies from remote spectroscopic measurements. Diviner data have been used to develop global maps of silicate composition and space weathering across the lunar surface. While low spectral sampling has prevented definitive determination of mineral composition, CF positions of lunar mare material have been observed to be consistent with a pyroxene-dominated mineralogy (Greenhagen et al., 2010), with olivine (Arnold et al., 2016), nearly pure

plagioclase (Donaldson Hanna et al., 2012), and other mineralogies (Glotch et al., 2010, 2011, 2015; Lucey et al., 2021; Song et al., 2013) detected as well.

The upcoming Lunar Trailblazer mission, which aims to understand the Lunar water cycle, is to be launched with NASA's Interstellar Mapping Acceleration Probe (IMAP) in 2025, and includes two spectrometers, the High-resolution Volatiles and Minerals Moon Mapper (HVM^3) and the Lunar Thermal Mapper (LTM). The HVM^3 instrument has a spectral range of 0.6–3.6 μm and has been optimized to quantify water. The LTM includes four temperature channels and 11 compositional channels targeting the Si-O CF, which represents a significant increase in compositional channels compared to Diviner's three. Overall, these instruments will provide an infrared and MIR map datasets with an increase in both spatial and spectral resolution compared to previous missions (Ehlmann et al., 2021).

2.2. Mars

In addition to pyroxene identification in Martian meteorites (Papike et al., 2009), analysis of VNIR and MIR wavelengths showed LCP and HCP to dominate much of the mineralogy of the low-albedo regions of Mars. Global compositional mapping of Mars from the Mars Global Surveyor Thermal Emission Spectrometer (MGS-TES) identified two surface types in dark regions defined by modal mineralogy: Surface Type 1, mostly composed of basalt, containing ∼25% CPX based on linear mixing models; and Surface Type 2, basaltic andesite or weathered basalt, with ∼10% CPX content (Bandfield, 2000). Expanding on this work, Rogers and Christensen (2007) and Rogers et al. (2007) reexamined low-albedo regions using TES data and identified 4 surface types based on modal mineralogical differences from region to region, including refined definitions for Surface Type 1 and 2. The distributions found in these studies are consistent with VNIR observations made using the Phobos 2 Imaging Spectrometer for Mars (ISM) by the Mars Express Observatoire pour la Minéralogie, l'Eau, les Glaces et l'Activité (OMEGA) VNIR data sets (Bibring, 2005; Bibring et al., 2006; Mustard et al., 1997). Both OPX and CPX are found in all 4 surface types (Rogers & Christensen, 2007).

2.3. Asteroids

McCord et al. (1970), interpreted the strong absorption band centered at 0.9 μm from telescope reflectance data (0.3–1.1 μm) of asteroid, four Vesta, as indicating a pyroxene-rich surface compositionally similar to basaltic achondrites. Subsequent studies found pyroxene to be a common surface component of S- and M-type asteroids (Chapman et al., 1975; Gaffey & McCord, 1978; Gaffey et al., 1993; Hardersen et al., 2005). Similarities between the spectral signature of Vesta and that of the howardite-eucrite-diogenite (HED) meteorites suggest Vesta to be the parent-body of HEDs (Drake, 1979; Feierberg & Drake, 1980; Gaffey, 1997). Recent support for this conclusion comes from spectral maps provided by the Visible and InfraRed (VIR) imaging spectrometer on the Dawn spacecraft. De Sanctis et al. (2012) provided geologic context for HED meteorites by highlighting the spectral differences with depth and across Vesta's surface with respect to HED compositions. The average spectral signature at global to regional scales is dominated by a howardite-like regolith containing localized regions with various proportions of eucrite (∼50% CPX) and diogenite (∼90% OPX) lithologies. VIR data of the Rhea Silvia Basin, a deeply excavated impact basin in the South Polar Region, indicates a larger amount of diogenite-like material at the surface suggesting diogenite may dominate at depth. Exogenous Vesta or Vesta-like material has also been detected on the near-Earth asteroid Bennu by the OSIRIS-REx OVIRS instrument, demonstrating the prevalence of asteroidal mixing processes in the inner solar system subsequent to planetary accretion (DellaGiustina et al., 2021).

Sunshine et al. (2004) demonstrated that high ratios of HCP/(HCP + LCP) are indicative of a differentiated body, using VNIR data collected at the NASA Infrared Telescope Facility (IRTF) and analyzed with the MGM. This was applied to several asteroids within the Merxia and Agnia S-type asteroid families and Thetis (S-type, non-family), all of which were found to have high HCP/(HCP + LCP) ratios (0.27–0.64) indicating they were derived from differentiated bodies.

Table 2
Sources and Compositions of Samples Used in This Study

Sample (abbreviations)	Sample source; locality	Composition	Chemical formula
Enstatite (En1)	SBU; Bamble, Norway	$En_{85}Fs_{14.5}Wo_{0.5}$	$Ca_{0.01}Mg_{1.71}Fe_{0.29}Al_{0.01}Si_{1.98}O_6$
Ferroan enstatite (Fen1)	SBU; Labrador, Canada	$En_{75.9}Fs_{22.7}Wo_{1.4}$	$Ca_{0.03}Mg_{1.47}Mn_{0.01}Fe_{0.44}Al_{0.15}Ti_{0.01}Si_{1.89}O_6$

2.4. Interplanetary, Cometary, Circumstellar, and ISM Dust

Enstatite (Mg-rich OPX) was observed in interplanetary dust particles collected from the Earth's stratosphere (Bradley et al., 1983; Mackinnon & Rietmeijer, 1987; Sandford & Walker, 1985), and in comets through ground-based IR observations (Hanner et al., 1994). Apart from these exceptions, however, it was commonly maintained that cosmic dust silicates are amporphous. Thus, much of the analytical work focused on deriving optical constants for glasses of pyroxene composition (Dorschner et al., 1995; Henning & Mutschke, 1997; Jäger et al., 1994). However, when the high-resolution MIR and FIR spectra from the Infrared Space Observatory (ISO) in the 2.5–240 μm wavelength range became available, crystalline pyroxenes were identified around young and evolved stars (Malfait et al., 1998; Molster et al., 2002), in the circumstellar disks of young stellar objects (Bouwman et al., 2001), and in planetary nebulae (Waters et al., 1998). With these new observations, it became apparent that there were insufficient high-resolution laboratory spectra of Mg-Fe silicates, against which to quantitatively interpret ISO data. Several studies were therefore undertaken to remedy this and understand the spectral properties of silicates, including olivine and pyroxene, across the ISO spectral range (Chihara et al., 2002; Jäger et al., 1998; Koike et al., 2000).

3. Methods

3.1. Sample Description and Preparation

Two large natural single crystal samples, enstatite (En1; Bamble, Norway) and ferroan-enstatite (Fen1; Labrador, Canada), were used for this study with an approximate size of 0.35–1 cm on a side (Table 2). Samples were loaned to us from the mineral collection at Stony Brook University, Department of Geosciences. Chemical compositions were determined by the Cameca SX100 electron microprobe at the American Museum of Natural History, New York. Thin sections of each sample were prepared to optically identify any possible exsolution or twinning that might affect IR data. While neither of these two samples exhibit any apparent twinning or exsolution, sample En1 does have parting parallel to the 001 plane. The IR spectra for En1 agree with oriented reflectance spectra for a natural enstatite ($En_{96}Fs_4$) reported by Jäger et al. (1998) and synthetic ortho-enstatite reported by Demichelis et al. (2012), indicating that the parting did not affect our spectral results.

Each sample was cut using a diamond saw blade to produce three different surfaces parallel to the *a*-plane (100), *b*-plane (010), and *c*-plane (001). Each surface was polished to a 0.25 μm surface roughness to provide a mirror-like surface. The orientations of these surfaces were confirmed through single-crystal X-ray diffraction measurements from which each crystal face was indexed. This analysis consisted of determining the unit cell and orientation matrix by the collection of a preliminary set of frames. From this, we indexed each crystal face using the CrysAlisPRO software. The reflections were collected using a four-circle κ Oxford Gemini diffractometer with an Atlas detector ($\lambda = 0.71073$Å) in the Department of Chemistry at Stony Brook University.

A portion of each sample was crushed and dry-sieved into four size fractions: <45, 45–63, 63–90, and 90–125 μm. The sieving process was repeated three or more times. Each grain size was washed in DI water to remove clinging fines from larger grains. Powder X-ray diffraction patterns were collected to assess sample purity using a Miniflex diffractometer with Cu$K\alpha$ radiation (λ = 1.54059 Å) and angle dispersive geometry, where data was collected in the 2θ 3–100°, with a step size of 0.02°, and continuous collection. A pressed pellet of 13 mm diameter and ∼1.5 mm thickness was made from the smallest size fraction of each sample.

3.2. Collection of VNIR, Mid- and Far- IR Reflectance Spectra

3.2.1. Mid- and Far-IR Spectra

We collected MIR specular reflectance spectra of oriented single crystals using the Stony Brook University Center for Planetary Exploration's Nicolet 6700 Fourier transform infrared (FTIR) spectrometer equipped with a FT-30 specular reflectance accessory with 30° incidence and emergence angles at a spectral sampling of 2 cm^{-1}. MIR spectra were measured using a KBr beamsplitter and a DTGS detector with a CsI window in the 400 to 4,000 cm^{-1} wavenumber range. FIR spectra were collected using a Nicolet Solid Substrate beam splitter and a DTGS detector with a polyethylene window in the 250 to 600 cm^{-1} wavenumber range. A total of 256 and 512 scans were averaged to produce the MIR and FIR spectra respectively. A KRS-5 holographic wire grid polarizer was placed in the path of the light source beam for the collection of polarized IR reflectance spectra for the single crystal samples. During analysis, the samples were placed on an aperture mask that controlled the spot size. The mask spot size was selected as the largest to be completely covered by the polished sample face. The two aperture sizes are approximately 4.7 and 6.8 mm and were used for Fen1 and En1 respectively. The underside of each mask was coated with paraffin soot prior to data collection to reduce light scattering from the mask. A background spectrum was acquired using a first surface gold mirror. A "blank" spectrum was also acquired of the empty mask and was subtracted from the mineral spectrum. The signal produced by the mask did not have a major effect in the MIR range, but a steep incline was observed beginning around 470 cm^{-1} increasing the reflectance from ~0.01 to ~0.11, as shown in Figure S1 in Supporting Information S1. We collected a total of 3 spectra per sample with the polarization direction parallel to each crystal axis (E||a, E||b, and E||c). The MIR and FIR spectra for each orientation were joined between 600 and 700 cm^{-1}, and the overlapping region was used to scale the FIR spectral contrast to be consistent with that of the MIR spectra.

The smallest grain size fraction for each sample was pressed into a powder pellet ~1.5 mm thick and 13 mm in diameter. Unpolarized MIR reflectance spectra of these pellets were collected using the same setup described for the MIR spectra of the oriented single crystal samples.

3.2.2. VNIR Spectra

VNIR reflectance spectra of the three largest size-fraction powders were measured using an ASD FieldSpec3 Max spectroradiometer using a 512 element Si photodiode array detector for the 0.35–1 μm (~28,571–10,000 cm^{-1}) range and two TE cooled InGaAs photodiode detectors for the 1–2.5 μm (~10,000–4,000 cm^{-1}) range. The samples were loaded into an aluminum sample cup painted flat black. The bottom of the sample cup was gently tapped on a table to level the powder's surface. Spectra of each size fraction for both samples were collected at 7 phase angles every 15° from 15° to 105° in the absence of ambient light, illuminated by a 50 W quartz halogen lamp, referenced to a calibrated Spectralon standard, and corrected for the non-Lambertian and wavelength-dependent nature of Spectralon following the methods of Yang et al. (2019). To reduce systematic error, the incident light source was kept at 45° to the sample, and the fiber optic bundle collecting the reflected light was adjusted on a goniometer to produce the desired phase angle. A total of four spectra were collected at each angle by turning the cup 90° for each collection to reduce error associated with possible preferred orientation of grains or uneven surface. The average of these four spectra was used in the model analysis discussed in Section 3.4.

3.3. Modeling of Mid-IR Oriented Optical Constants

MIR optical constants were derived using a combination of Lorentz-Lorenz dispersion theory and a Fresnel reflectance model (Glotch et al., 2007). Dispersion theory mathematically defines the vibrational transitions within a mineral as the summation of lattice harmonic oscillators. Each oscillator is described by a set of parameters, ν, $4\pi\rho$, and γ, which are the center frequency of oscillation, the band strength, and the band width, respectively. An additional term, the high frequency dielectric constant (ε_0), is a bulk property and can be approximated as n^2_{vis} (Roush et al., 1991). The real (n) and imaginary (k) indices of refraction can be described as a function of these parameters by the following equations:

$$n^2 - k^2 = \varepsilon_0 + \sum_j \frac{4\pi\rho_j\nu_j^2\left(\nu_j^2 - \nu^2\right)}{\left(\nu_j^2 - \nu^2\right)^2 + \left(\gamma_j^2\nu_j^2\nu^2\right)} \quad (1)$$

$$nk = \sum_j \frac{4\pi\rho_j \nu_j^2 (\gamma_j \nu_j \nu)}{\left(\nu_j^2 - \nu^2\right)^2 + \left(\gamma_j^2 \nu_j^2 \nu^2\right)} \tag{2}$$

The optical constants are then related to the total reflectance by the Fresnel equations, which describe the total reflectance for non-normal incidence angles (Glotch et al., 2007):

$$R_T = \frac{R_\perp^2 + R_\parallel^2}{2} \tag{3}$$

$$R_\parallel^2 = \frac{(\cos\theta - u)^2 + v^2}{(\cos\theta + u)^2 + v^2} \tag{4}$$

$$R_\perp^2 = \frac{\left[\left(n^2 - k^2\right)\cos\theta - u\right)\right]^2 + (2nk\cos\theta - v)^2}{\left[\left(n^2 - k^2\right)\cos\theta + u\right)\right]^2 + (2nk\cos\theta + v)^2} \tag{5}$$

$$u = \left(\frac{n^2 - k^2 - sin^2\theta + \left[\left(n^2 - k^2 - sin^2\theta\right)^2 + 4n^2k^2\right]^{1/2}}{2} \right)^{1/2} \tag{6}$$

$$v = \left(\frac{-\left(n^2 - k^2 - sin^2\theta\right) + \left[\left(n^2 - k^2 - sin^2\theta\right)^2 + 4n^2k^2\right]^{1/2}}{2} \right)^{1/2} \tag{7}$$

We used Matlab non-linear least squares optimization routine to iteratively fit measured spectra. Initial guesses for the parameters ε_0, ν, $4\pi\rho$, and γ, were estimated through visual inspection of spectral features and input into the model. These values were then used in the model to iteratively fit the measured spectrum and calculate n and k values, which were used to calculate a modeled reflectance spectrum using the Fresnel relationships shown above in Equations 3 through 5. The model output includes optimized values of the input parameters, a calculated reflectance spectrum, n, and k. The optical constants are derived when a reasonable fit (<10% difference from model) of the measured spectrum is achieved using the least number of oscillators possible (Spitzer & Kleinman, 1961).

3.4. Modeling of VNIR Optical Constants

VNIR optical constants were derived following a modified procedure from Sklute et al. (2015, 2021). This model utilizes the Hapke treatment of radiative transfer combined with Kramers-Kronig transformations to iteratively fit measured spectra and obtain bulk values for n and k over the VNIR wavelength range (0.35–2.5 μm).

The reflectance is calculated from:

$$REFF(i,e,g) = K\frac{w}{4}\frac{1}{\mu_0 + \mu}\left[p(g) + H\left(\frac{\mu_0}{K}\right)H\left(\frac{\mu}{K}\right) - 1\right] \tag{8}$$

where *REFF* is the reflectance of the sample ratioed to the reflectance of a Lambertian scatterer viewed at the same angle, K is the porosity factor, μ is the cosine of the emission angle, μ_0 is the cosine of the incidence angle, w is the single scattering albedo, $p(g)$ is the phase function, and H(x) is the Ambartsumian-Chandrasekhar's H-function.

The phase function, $p(g)$, represents the phase angle dependence of singly scattered light and is modeled with a two term Legendre polynomial:

$$p(g) = 1 + b\cos(g) + c\left[1.5\cos^2(g) - 1.5\right] \tag{9}$$

where g is the phase angle (the sum of the incidence and emission angles), and b and c are the phase function coefficients.

The measured radiance is related to n and k through the single scattering albedo, w, which is described as follows for closely packed particles:

$$w = S_e + (1 - S_e)\frac{(1 - S_i)}{1 - S_i\Theta}\Theta \tag{10}$$

where Θ, S_e and S_i are the internal transmission factor and Fresnel reflectance coefficients, respectively. The internal transmission factor, Θ, takes into account the effective grain size D, that is, the path length traveled by light through a grain, the absorption coefficient ($\alpha = 4\pi k/\lambda$), and the internal scattering factor, s, such that,

$$\Theta = \frac{r_i + \exp(-\sqrt{\alpha(\alpha + s)}\langle D\rangle)}{1 + r_i \exp(-\sqrt{\alpha(\alpha + s)}\langle D\rangle)} \tag{11}$$

$$r_i = \frac{1 - \sqrt{\alpha/(\alpha + s)}}{1 + \sqrt{\alpha/(\alpha + s)}} \tag{12}$$

The Fresnel reflectance coefficients (Equation 10) are integrated over all angles and can be described as a function of n and k as follows:

$$S_e \approx \frac{(n - 1)^2 + k^2}{(n + 1)^2 + k^2} + 0.05 \tag{13}$$

$$S_i \approx 1.014 - \frac{4}{n(n + 1)^2} \tag{14}$$

The Ambartsumian-Chandrasekhar's H-function can be approximated by

$$H(x) \approx \left\{1 - wx\left[r_0 + \frac{1 - 2r_0x}{2}\ln\left(\frac{1 - x}{x}\right)\right]\right\}^{-1} \tag{15}$$

or its exact solution can be determined using a lookup table approach. For highly reflective materials, the exact solution is necessary for good convergence. For the samples in this study, the approximation (Equation 15) was used.

The greatest challenge to modeling the VNIR optical constants is that without additional constraints, one can derive a model (Equation 8) which appears to approximate the data well using multiple mathematically equivalent solutions for variables $n(\lambda)$, $k(\lambda)$, b, c, D, and s, providing non-unique solutions, many of which might not be physically reasonable. Following Sklute et al. (2015), we used spectra of three grain sizes at 7 phase angles each to derive the intrinsically wavelength and grain size independent optical constants n and k. However, we reordered the steps in a manner similar to Yang et al. (2019) as outlined in Sklute et al. (2021) to ensure that phase behavior is completely described by phase function coefficients, thus obtaining a more robust solution for k. The procedure is as follows:

1. Because each grain size has one single scattering albedo, w, at each wavelength, all phase angle spectra for each grain size can be modeled using the same w, thus forcing all phase behavior to be accounted for by the phase function coefficients b and c. Once wavelength dependent b and c are determined for each grains size through this step, they are considered known quantities for the remainder of the derivation.
2. The single scattering albedos from the three grain sizes viewed at a single-phase angle (typically $g = 30°$, although solutions from all phase angles at this stage are compared to look for systematic variations), along with a constant n obtained from the average value n at the sodium D line, are used to derive a wavelength-dependent value of k. We thus force all variation between the spectra of different grain sizes to be accounted for by effective grain size and internal scattering coefficient (Equations 10–15).
3. The derived VNIR k is combined with the MIR k and a Singly Subtractive Kramers-Kronig (SSKK) transformation is used to derive the wavelength-dependent VNIR n:

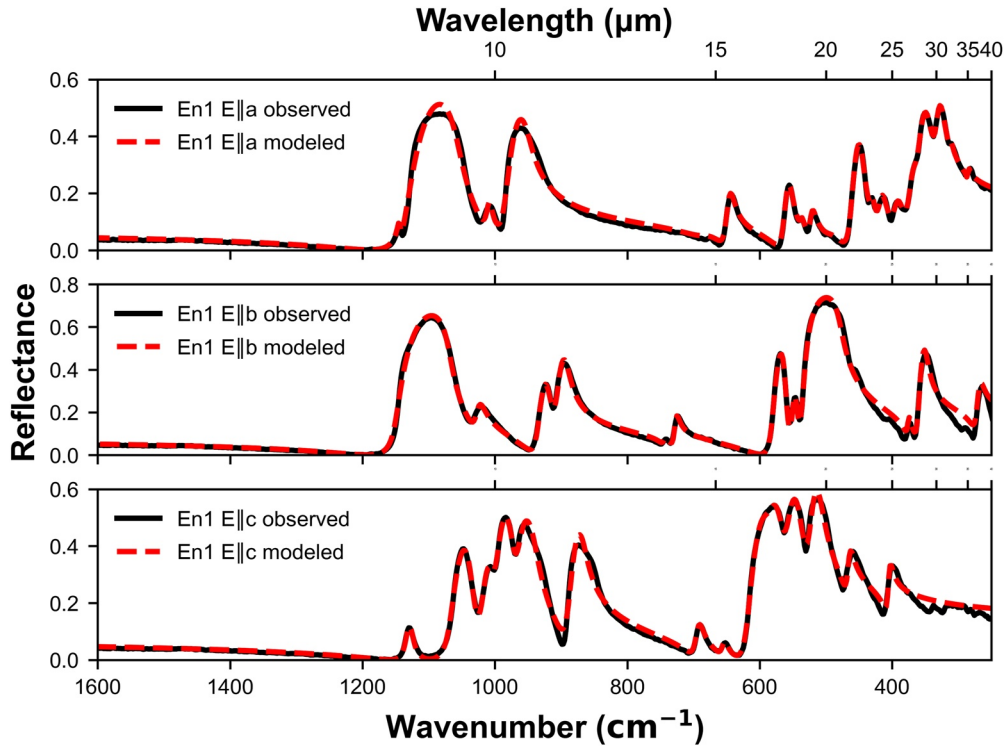

Figure 1. Measured and modeled Mid-IR reflectance spectra of enstatite (En1) with E-field polarization parallel to the a- (top), b- (middle), and c- axis (bottom).

$$n(\lambda) = n(\lambda_0) + \frac{2\left(\lambda^2 - \lambda_0^2\right)}{\pi} \times P \int_0^{\infty} \frac{\lambda' k(\lambda')}{\left[\lambda^2 - (\lambda')^2\right]\left[\lambda_0^2 - (\lambda')^2\right]} d\lambda' \tag{16}$$

While the SSKK transformation ideally needs an infinite data range to converge to a unique solution, this condition is never met. Sklute et al. (2015) demonstrated that extending the data range in the MIR for calculation of VNIR optical constants results in substantially different n values than if only the VNIR range is used. Here, we extend the k data to the MIR by modeling the pressed pellet spectrum (effectively averaging over all possible orientations) in the same manner as the oriented spectra.

4. The wavelength dependent n is used in the minimization procedure to derive a new k and these steps are iterated several times until there is negligible variation between iterations.

4. Results

Here we provide the observed and modeled near-IR and mid- to far-IR reflectance, as well as the calculated values of n and k for both samples. All spectra and derived optical constants are available at https://doi.org/10.5281/zenodo.4758045

4.1. Mid-IR Oriented Optical Constants

The oriented observed and modeled reflectance spectra for enstatite (En1) are shown in Figure 1, where the incident polarization directions are parallel to the axes of symmetry of the crystal, *a*- (top), *b*- (middle), and *c*- (bottom), denoted by E ∥ a, E ∥ b, and E ∥ c respectively. The derived n and k values for all three polarization directions are shown in Figure 2. Oscillator parameters for enstatite at all three orientations are shown in Table 3.

The oriented observed and modeled reflectance spectra for ferroenstatite (Fen1) are shown in Figure 3. The derived n and k values for all three polarization directions are shown in Figure 4. Oscillator parameters for

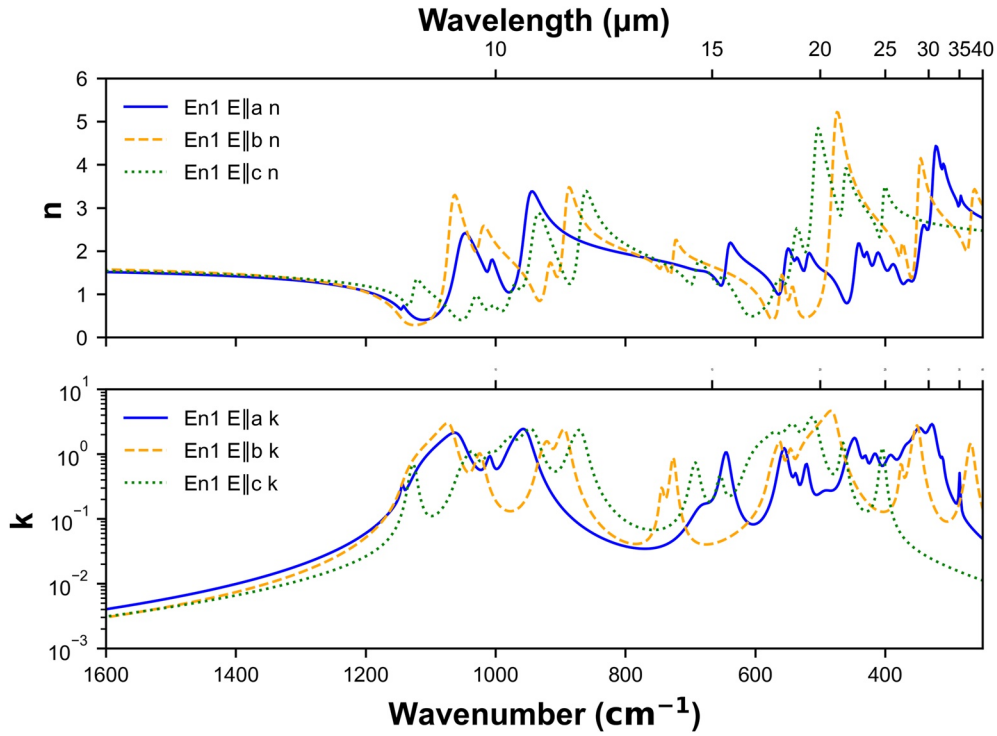

Figure 2. Mid-infrared optical constants, n and k, of enstatite (En1).

enstatite at all three orientations are shown in Table 4. The fit for the ferroenstatite MIR E ‖ b has some misfit at low wavenumbers. The spectrum was best fit with an oscillator at the end of the available data: there may be an oscillator here, but without an extended spectrum this in unconfirmed and is reported here with caution.

4.2. VNIR Optical Constants

Observed and modeled reflectance for all three grain sizes of En1 in the VNIR are shown in Figure 5. For clarity, only fits for a phase angle of 45 are shown. Fits for all other phase angles are shown in Figure S2 in Supporting Information S1. The derived optical constants, *n* and *k*, are shown in Figure 6

Observed and modeled reflectance for all three grain sizes of Fen1 in the VNIR are shown in Figure 7, for clarity, only fits for a phase angle of 45 are shown. Fits for all other phase angles are shown in Figure S3 in Supporting Information S1. The derived optical constants, *n* and *k*, are shown in Figure 8.

5. Discussion

5.1. Comparison With Previously Derived Orthopyroxene Optical Constants

5.1.1. MIR

The typical approach taken for deriving optical constants in the MIR, particularly in the case of poorly crystalline materials, that is, clays and iron oxides (Glotch & Rossman, 2009; Roush et al., 1991), involves deriving *n* and *k* from reflectance spectra of pressed pellets. These optical constants were assumed to be the average of all principal indices of refraction. While this is a good approximation, it is not completely accurate, as can be seen in Figure 9 where we show the average of all three oriented indices of refraction calculated here for En1 set against the calculated *n* and *k* from a pressed pellet of the same sample. Specifically, *n* and *k* values for the pressed pellet tend to be lower than the average of the three orientations of the single crystal by a factor of ∼2 in the Reststrahlen band region. From the standpoint of deriving VNIR optical constants, the most important feature of the MIR *k* is its magnitude near 2.5 μm, as this has the greatest effect on the degree to which VNIR *n* decreases with λ.

Earth and Space Science

10.1029/2021EA002104

Table 3
Oscillator Parameters for Enstatite

	E II a						E II b						E II c					
j	ν_j	$\sigma(\nu_j)$	γ_j	$\sigma(\gamma_j)$	$4\pi\rho$	$\sigma(4\pi\rho)$	ν_j	$\sigma(\nu_j)$	γ_j	$\sigma(\gamma_j)$	$4\pi\rho$	$\sigma(4\pi\rho)$	ν_j	$\sigma(\nu_j)$	γ_j	$\sigma(\gamma_j)$	$4\pi\rho$	$\sigma(4\pi\rho)$
1	1143.0000	0.4077	4.5424	1.1891	997.3800	183.6500	1068.8000	0.2455	19.5150	0.2463	318000.0000	3920.5000	1125.2000	0.4538	11.7980	0.9825	19780.0000	1139.5000
2	1055.7000	0.2272	30.8630	0.2912	260000.0000	2316.4000	1023.0000	0.5206	15.7310	1.5174	64803.0000	4711.8000	1033.0000	0.2175	19.0000	0.5289	29431.0000	899.6500
3	1007.9000	0.3911	10.2900	1.1069	18644.0000	1445.6000	918.6800	0.2827	15.3870	0.7625	53969.0000	2923.7000	1004.6000	0.3733	19.3370	1.5536	15418.0000	1215.2000
4	952.1500	0.2499	24.8260	0.3991	304000.0000	2643.4000	891.6500	0.2833	15.4980	0.6491	180000.0000	4270.4000	973.6100	0.2777	18.3190	0.9710	45989.0000	2695.7000
5	681.6200	5.0588	40.2450	17.0830	8979.7000	3218.1000	743.7500	1.2642	7.5310	3.9439	4179.1000	1649.1000	940.8300	0.2607	24.8770	0.6738	255000.0000	3873.8000
6	643.2200	0.2984	12.8180	0.7884	30998.0000	1609.7000	725.5500	0.3849	8.5478	1.0123	20611.0000	1822.1000	867.1900	0.2582	19.2500	0.4545	207000.0000	2766.1000
7	553.4400	0.2491	13.0150	0.5670	28721.0000	1167.3000	560.5500	0.1510	8.3304	0.3046	15599.0000	452.7700	690.9500	0.4995	13.7570	1.2543	19884.0000	1299.0000
8	537.3500	0.7572	7.1345	2.7311	3491.4000	1149.5000	544.2600	0.2191	8.7563	0.6303	8615.0000	421.6300	653.3000	0.8831	10.8510	2.5132	6458.6000	1100.3000
9	520.5200	0.4149	9.9838	1.4455	10642.0000	1435.7000	478.9900	0.2541	16.9010	0.2717	304000.0000	1816.9000	588.0300	2.0601	26.6050	3.8217	8832.9000	3050.3000
10	493.4500	3.9134	34.7360	11.5440	7807.0000	2422.5000	374.9500	0.4446	5.4760	1.3281	4404.2000	750.3600	567.0500	0.3957	22.1970	2.0679	45161.0000	5115.7000
11	444.4200	0.2189	13.8470	0.4541	36238.0000	1218.1000	348.9200	0.2205	10.0450	0.3633	63192.0000	1314.5000	539.0800	0.2449	19.9410	0.9610	114000.0000	5416.7000
12	429.9200	0.4721	7.6176	1.8527	5435.2000	1295.1000	266.8500	0.3230	10.8480	0.7684	24237.0000	1273.6000	508.4700	0.2344	16.7290	0.5822	234000.0000	4493.3000
13	414.3800	0.4131	14.8550	1.7195	16786.0000	1864.0000							463.6300	0.2870	9.6794	0.7786	41030.0000	2328.7000
14	390.5800	0.5177	18.7200	2.2325	15339.0000	1881.9000							403.3800	0.2431	7.7227	0.6041	23347.0000	1272.9000
15	366.2500	0.6269	17.4480	2.9712	9782.3000	2222.7000												
16	344.3600	0.3020	18.2470	1.1660	59442.0000	4504.0000												
17	325.5400	0.2206	12.9820	0.8314	81306.0000	4522.5000												
18	311.3000	0.6908	4.8287	2.1778	4375.9000	1770.6000												
19	285.1600	0.2062	1.8589	2.9028	1318.7000	601.1300												
$\varepsilon_{0,\,EIIa} = 2.8021\ (0.0057)$							$\varepsilon_{0,\,EIIb} = 3.0656\ (0.0083)$						$\varepsilon_{0,\,EIIc} = 2.9189\ (0.0068)$					

Note. Oscillators are listed for EIIa, EIIb, EIIC separately. The standard error (σ) is given with each parameter.

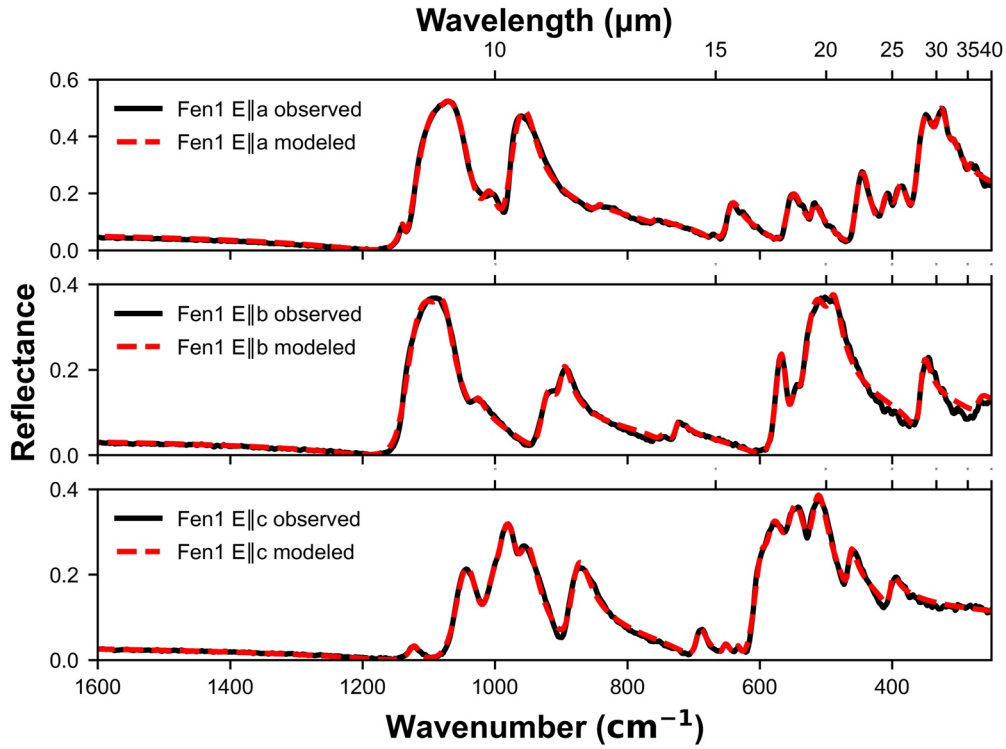

Figure 3. Measured and modeled Mid-infrared reflectance spectra of ferroenstatite (Fen1) with E-field polarization parallel to the a- (top), b- (middle), and c- axis (bottom).

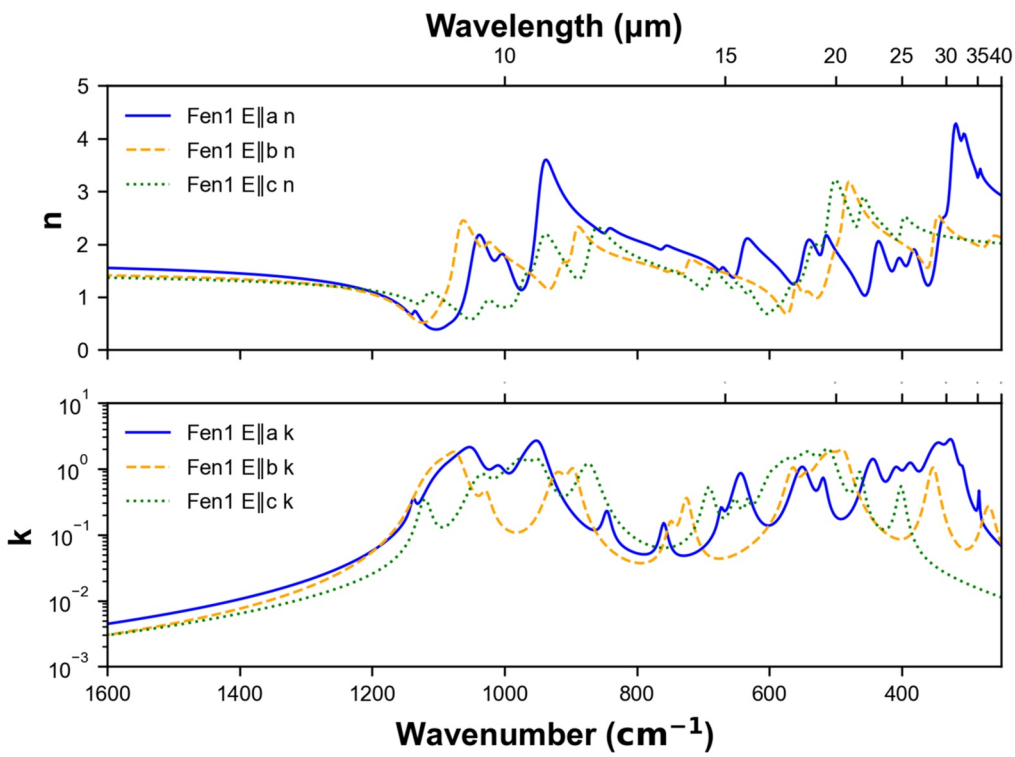

Figure 4. Mid-infrared optical constants, n and k, of ferroenstatite (Fen1).

Earth and Space Science

10.1029/2021EA002104

Table 4
Oscillator Parameters for Ferroenstatite

E II a							E II b						E II c					
j	ν_j	$\sigma(\nu_j)$	γ_j	$\sigma(\gamma_j)$	$4\pi\rho$	$\sigma(4\pi\rho)$	ν_j	$\sigma(\nu_j)$	γ_j	$\sigma(\gamma_j)$	$4\pi\rho$	$\sigma(4\pi\rho)$	ν_j	$\sigma(\nu_j)$	γ_j	$\sigma(\gamma_j)$	$4\pi\rho$	$\sigma(4\pi\rho)$
1	1137.1000	0.3124	8.1191	0.9537	2073.0000	188.2300	1092.7000	1.4354	38.5530	1.5854	43750.0000	7259.5000	1118.9000	0.7112	19.5460	2.0014	12640.0000	956.6800
2	1084.4000	1.5025	20.8080	4.8133	2443.0000	809.1000	1070.6000	0.2464	26.4180	0.9821	186000.0000	7858.8000	1029.5000	0.3232	31.5640	0.7954	33696.0000	1651.7000
3	1045.8000	0.1509	30.1630	0.4384	223000.0000	3049.3000	1027.7000	0.7396	16.8520	2.4600	19195.0000	2410.3000	999.3600	1.0748	32.5140	5.7613	13740.0000	3767.5000
4	1007.2000	0.3459	25.4740	1.1720	59361.0000	2553.4000	917.1300	0.5366	27.4010	1.4279	54311.0000	3932.8000	972.1600	0.2929	26.5020	1.5149	60029.0000	5238.4000
5	946.3600	0.1633	26.4480	0.2892	373000.0000	2087.9000	894.6300	0.3060	18.2000	1.1416	56333.0000	3726.0000	946.4300	0.2670	29.5310	0.8050	127000.0000	3913.5000
6	845.1700	1.0491	13.2640	3.1174	7921.7000	1377.0000	748.8500	2.0809	14.3180	6.8819	3356.3000	1322.0000	869.5700	0.2012	28.6520	0.4825	110000.0000	1325.2000
7	759.3000	1.4131	12.1630	4.0865	3915.8000	959.8800	724.4000	0.6624	15.2970	2.1450	11566.0000	1393.7000	689.8100	0.3669	17.3210	1.0099	14860.0000	648.2000
8	672.6600	1.1219	8.4881	3.4352	2171.0000	678.1100	562.1000	0.2071	13.3450	0.5608	12223.0000	720.0400	651.6600	0.7304	13.7250	2.4488	4737.5000	675.5900
9	641.1500	0.2781	21.3970	0.7629	40951.0000	1074.7000	544.0700	0.6088	20.5820	2.8593	8879.2000	1523.0000	632.3300	0.6959	7.2574	2.1650	1512.6000	369.9400
10	547.4500	0.2404	24.2770	0.6407	47894.0000	1058.4000	504.8700	0.8299	34.3560	1.6130	78488.0000	7704.7000	592.7600	0.5645	18.1150	2.4066	4083.5000	996.7500
11	517.8100	0.2922	11.7870	0.9310	13355.0000	863.4700	485.8500	0.2913	19.6500	1.1242	78095.0000	6192.8000	569.4100	0.3485	32.2200	2.0003	37210.0000	3332.8000
12	440.6600	0.1602	19.2940	0.3909	37602.0000	670.0200	351.2000	0.2213	15.2840	0.5193	23441.0000	570.1600	538.6500	0.2235	30.0910	1.1822	79399.0000	4024.9000
13	407.4200	0.3236	18.7710	1.2538	17124.0000	1253.0000	268.4400	0.9155	20.5120	3.1891	5703.4000	763.9700	507.9900	0.1595	23.7430	0.5352	116000.0000	2423.6000
14	385.3600	0.2764	20.3530	0.9888	24319.0000	1223.5000							462.5900	0.1919	12.2440	0.5637	21921.0000	766.4700
15	342.4700	0.3194	22.2740	0.6682	62708.0000	3465.5000							400.6300	0.2638	12.6710	0.7460	11584.0000	501.4200
16	323.5300	0.1883	16.1650	0.8683	92082.0000	5180.5000												
17	307.9000	0.5222	8.9309	1.8175	10846.0000	2378.5000												
18	283.3600	0.2224	2.0985	2.2463	1152.1000	439.0600												
$\varepsilon_{0,\,EIIa} = 2.9796$ (0.0037)							$\varepsilon_{0,\,EIIb} = 2.3222$ (0.0039)						$\varepsilon_{0,\,EIIc} = 2.2132$ (0.0029)					

Note. Oscillators are listed for EIIa, EIIb, EIIC separately. The standard error (σ) is given with each parameter.

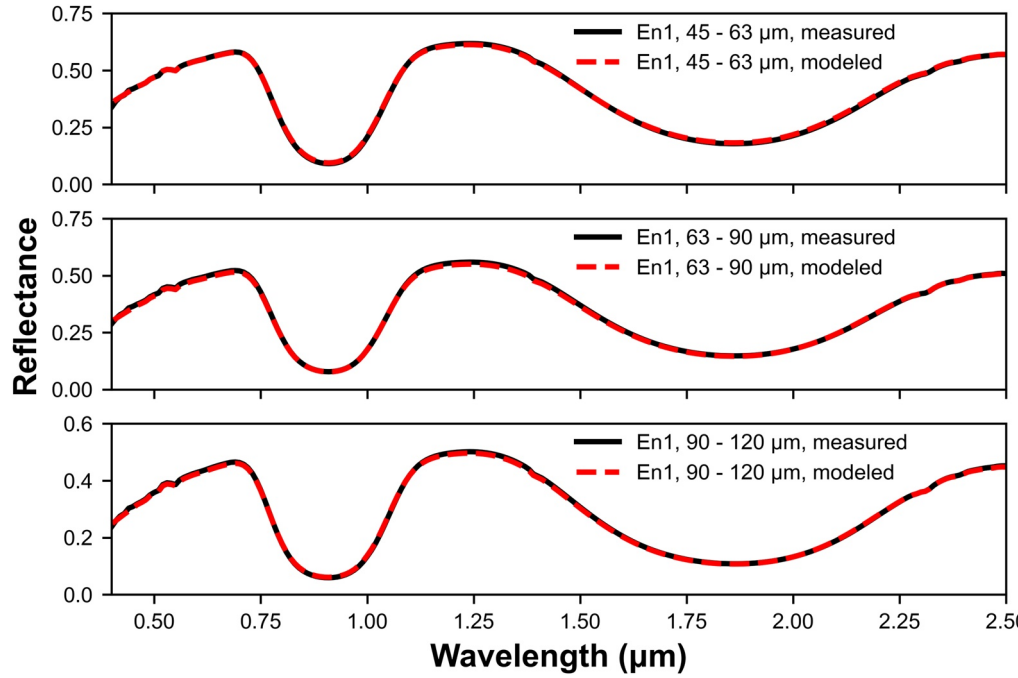

Figure 5. Measured and modeled Visible to Near-Infrared reflectance spectra of enstatite (En1) at g = 45° for grain sizes 45–53 μm (top), 63–90 μm (middle), and 90–120 μm (bottom).

There has only been two previously reported oriented optical constants derived for orthopyroxene previously reported in the literature (Jäger et al., 1998; Zeidler et al., 2015). Jäger et al. (1998) used a Kramers-Kronig analysis to calculate the *n* and *k* optical constant values for a natural single crystal of enstatite ($En_{96}Fe_4Wo_0$). In Figure 10, we show a comparison of the *n* and *k* for enstatite in this study (En1) and that reported in Jäger

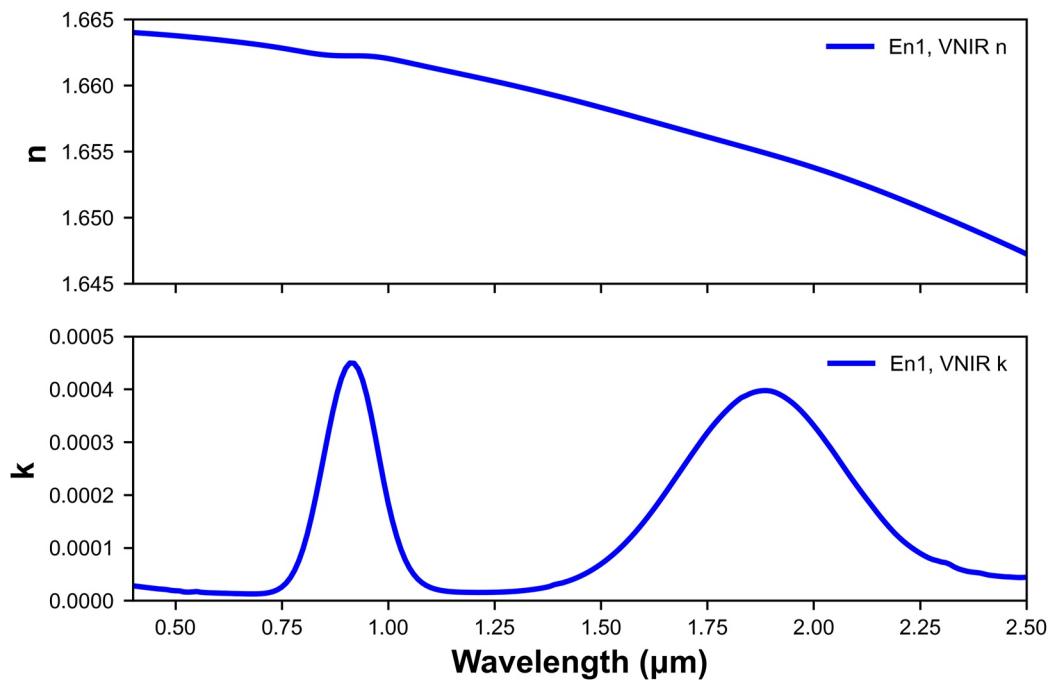

Figure 6. Average Visible to Near-Infrared optical constants, n and k, of enstatite (En1). Separate n and k values were calculated for every phase angle and averaged to find the reported value.

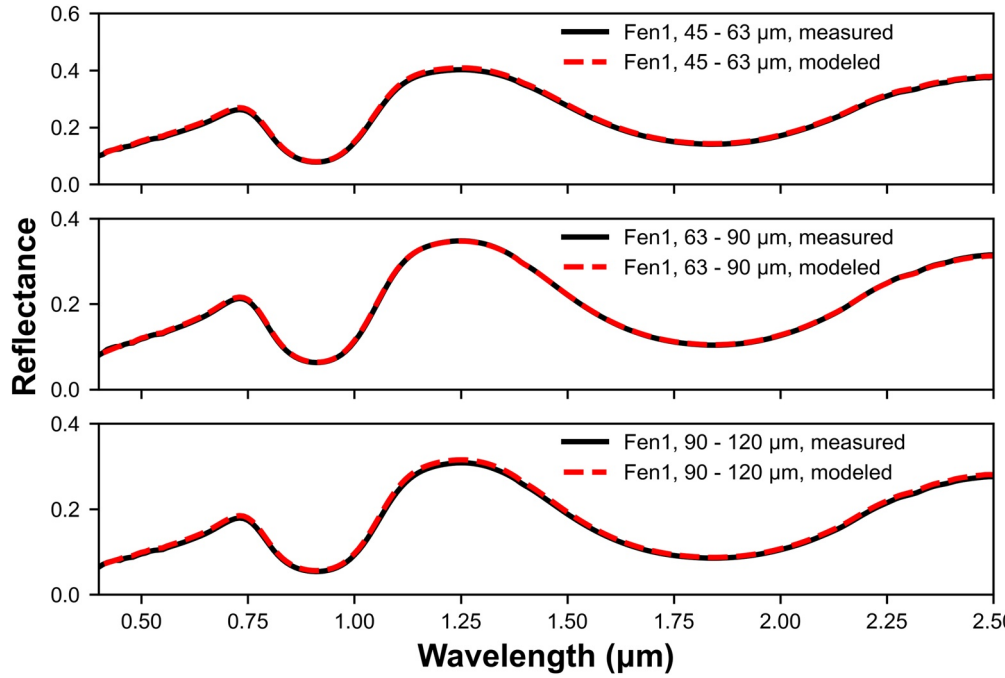

Figure 7. Measured and modeled Visible to Near-Infrared reflectance spectra of ferroenstatite (Fen1) at g = 45° for grain sizes 45–53 µm (top), 63–90 µm (middle), and 90–120 µm (bottom).

et al. (1998) for the E||c orientation. Our *n* values are consistent with Jäger et al. (1998) with the exception of slight shifts in peak position and peak height, which is likely due to the differences between the enstatite sample compositions. We note a greater difference between the *k* values. While the *k* values are similar within the 400–1,200 cm^{-1} range, in regions where *k* is small, the values differ by ∼2 orders of magnitude, indicating the Kramers-Kronig approach may overestimate *k* values in the transparent regions.

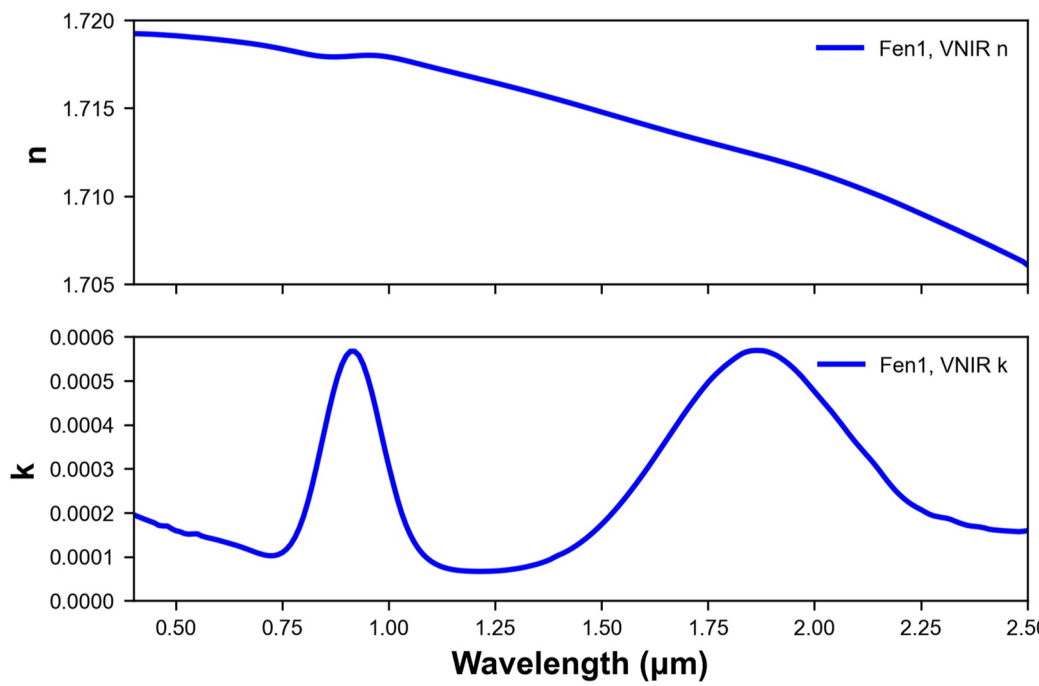

Figure 8. Average Visible to Near-Infrared optical constants, n and k, of ferroenstatite (Fen1). Separate n and k values were calculated for every phase angle and averaged to find the reported value.

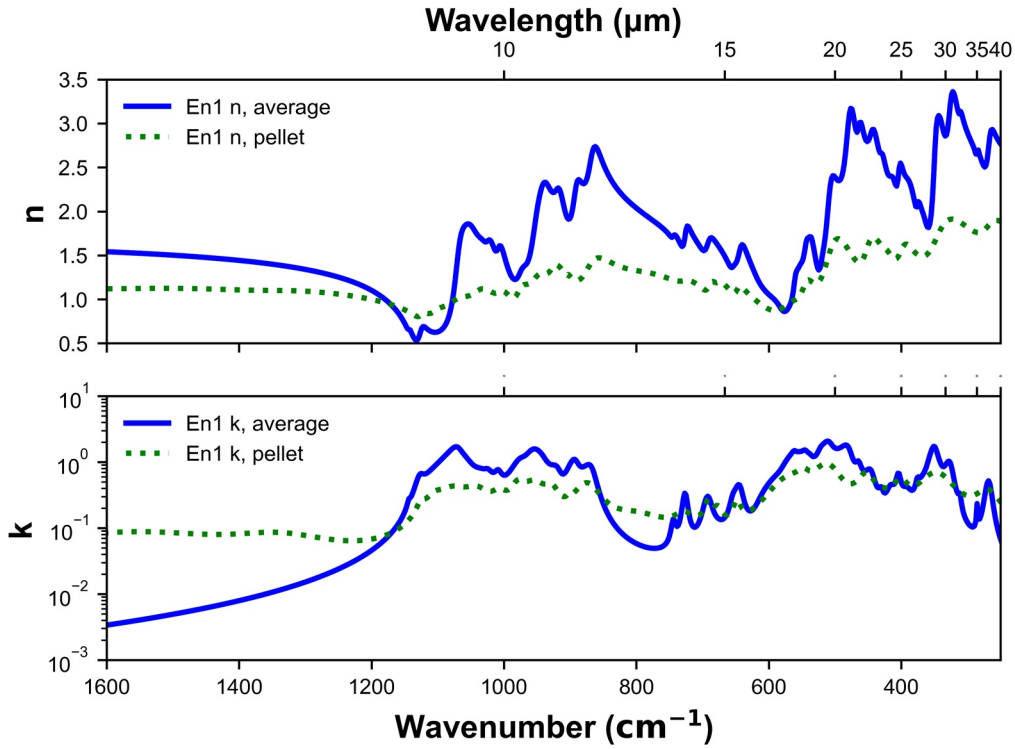

Figure 9. Comparison between enstatite (En1) optical constants, n and k, from the average of the oriented Mid-IR values (blue, solid), and values calculated using a pressed powder pellet of the same sample (green, dotted).

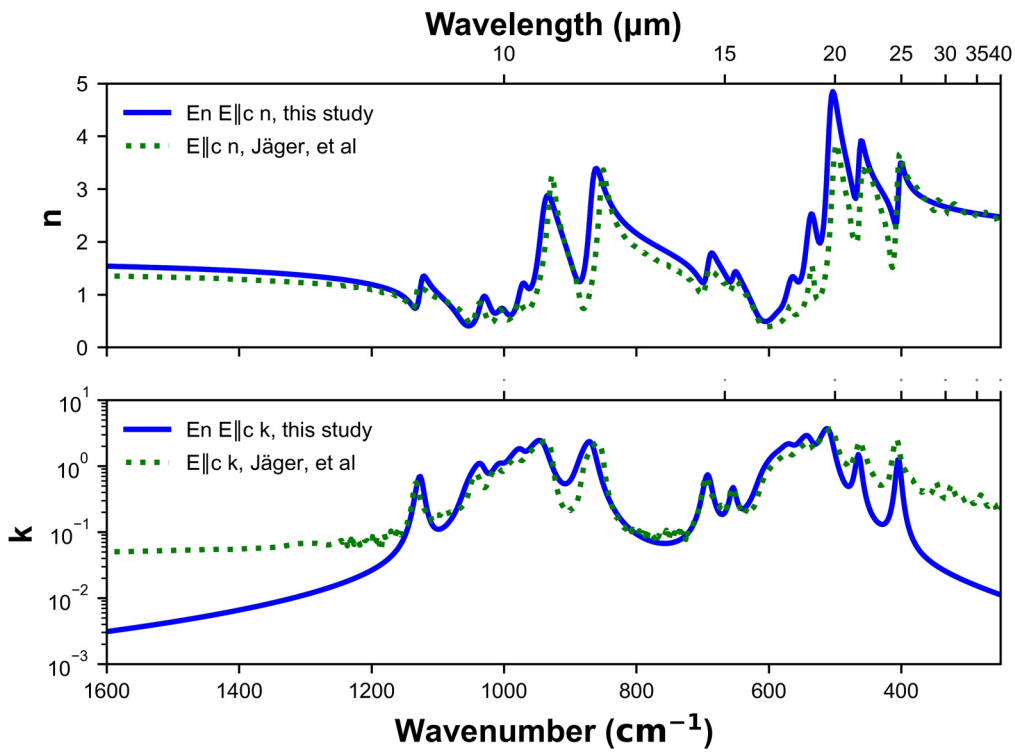

Figure 10. Comparison of enstatite optical constant, *n* and *k*, with E-light polarization parallel to the c-axis (blue, solid) with optical constants reported for oriented enstatite of similar composition (green dotted), reported in Jäger et al. (1998).

(Zeidler et al., 2015) investigated the temperature dependance of oriented optical constants of orthoenstatite (En_{92}) using a Lorentz oscillator model over a spectral range of 5–60 μm (~150–2,000 cm^{-1}). The oscillator ν_j positions presented here are in good agreement with those reported in Zeidler et al. (2015), although some shifting of this parameter is present. This may be due to compositional effects that are expected to shift the oscillator positions systematically with increasing iron content as observed in bulk emissivity data (Hamilton, 2000). While beyond the scope of this study, the compositional effect to individual oscillator parameters is of interest.

5.1.2. VNIR

Other studies have derived k values for OPX by converting NIR diffuse reflectance data to k spectra using different relations (Lucey, 1998) or converting spectra to k using MGM (Denevi et al., 2007; Trang et al., 2013). There are four key differences between the methodology used here and those that have been previously reported. First, in other studies, the k values are derived for each grain size individually and averaged together. By simultaneously fitting our multiple grain size data to derive a single k spectrum, we arrive at a more accurate solution for a grain size independent imaginary index of refraction. Second, the wavelength-dependent n is also calculated here, whereas previous studies have assumed this to be constant. While the change in n across this spectral region is small, we have shown here there is some variation of n with wavelength (Figure 6). Third, in our calculations of VNIR optical constants, we extended the data range to the MIR to reach a more convergent and correct solution for the SSKK transformation (Sklute et al., 2015). Finally, and most importantly, we have leveraged the fact that grain size contributions and phase behavior contributions are mathematically separable using Hapke theory in order to separate phase function determination from optical constant determination. Other studies assumed either that phase behavior is isotropic or have chosen constant values for the phase function coefficients, which forces any variation due to phase behavior to be accounted for by the optical constants themselves. Thus, our calculated n and k in the VNIR are more robust than previous estimates.

5.2. Model Errors

5.2.1. Mid-IR

Following Arnold et al. (2014), we assessed the MIR dispersion model fits using standard error for each of the oscillator parameters and reported the errors in Tables 3 and 4 for En1 and Fen1 respectively. The inherent error associated with the parameters used to calculate the final n and k values was estimated by shifting the parameter values by ±20 cm^{-1} for ν_j and ±50% for others. Little to no change is seen in the resulting n and k values. Representative spectra of the resulting n and k for En1 Ella with the parameter changes are shown in Figures S4–S7 in Supporting Information S1. With each change there are only minor differences that are associated with smaller or clumped spectral features.

5.2.2. VNIR

The assumptions we made in our approach to simplify the manner in which we mathematically describe these material properties allowed us to achieve a great fit for the VNIR reflectance data, shown in Figures 5 and 7 and Figures S2 and S3 in Supporting Information S1, adding confidence in the calculated k values. Minimal misfit is observed in the UV region, see Figures S2 and S3 in Supporting Information S1, likely due to the extension of data into this region through a linear fit rather than direct measurement.

In order to assess the accuracy of the model, k values were calculated for each phase angle individually (see step 2 in model outline) and compared in Figure 11. There are two major features in the spectra at ~0.9 and ~1.9 microns. The positions of the maxima do not shift, however the k values vary with phase angle, across the entire spectral range, with the greatest shift observed at the maxima. According to Equations 10–14, k values are independent of phase angle, thus no variation should be observed. The difference in intensity in Figure 11 seems to be loosely correlated with phase angle, where the smallest and largest phase angles have lower calculated k values than for those that are in the mid-range of phase angles used here. We observe inverse behavior in the measured reflectance spectra. Figure 12 shows a comparison of k value and the reflectance for all grain sizes at the ~0.9 μm maximum for both En1 and Fen1, where a pseudo-parabolic relationship between the phase angle and reflectance can be seen (additional data are shown in Figure S8 in Supporting Information S1).

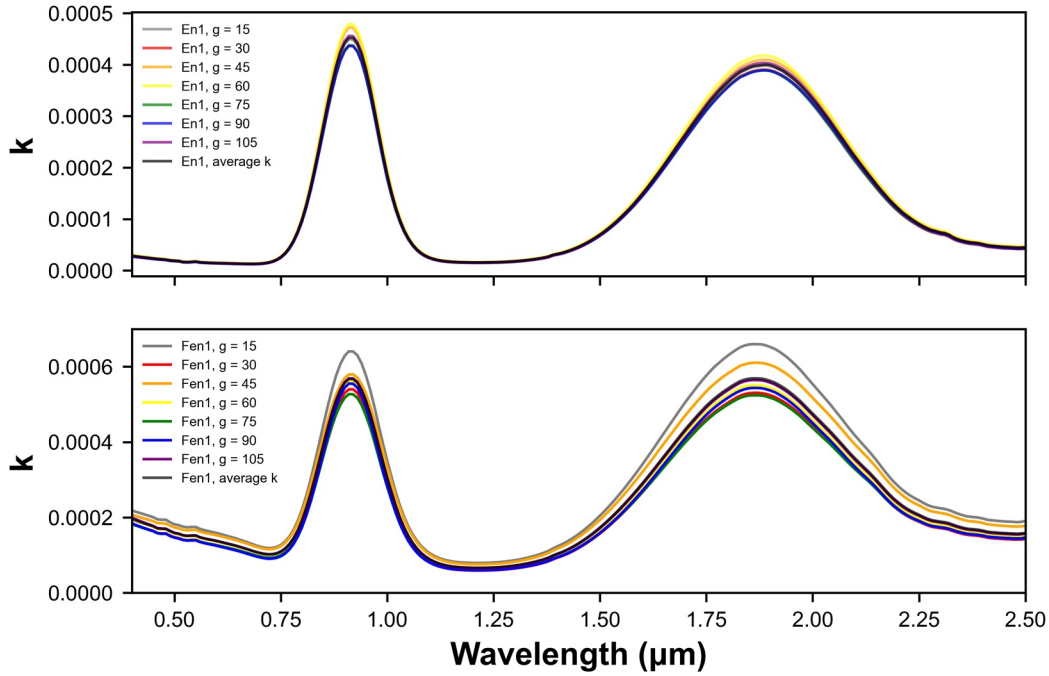

Figure 11. Individual calculated k values at each phase angle for enstatite (top) and ferroenstatie (bottom).

A possible explanation for this behavior is that the Spectralon is an isotropic scatterer, rather than a Lambertian scatterer (Sklute et al., 2015). An isotropic scatterer would have a higher reflectance at mid phase angles and a lower reflectance at high and low phase angles with respect to a Lambertian scatterer (Piatek, 2003; Sklute et al., 2015). The model would, therefore, attribute more reflectance to samples with respect to the standard at mid phase angles. This would result in a systematic difference in the value of *k* at all wavelengths, which is what we observe here for both En1 and Fen1, however may not account completely for the greater degree of spread in *k* value at the feature maxima.

Additionally, both the single scattering albedo and the *k* solution are influenced by the calculated grain size values, which may contribute to this affect. These values are calculated within our model and are allowed to vary within lower and upper bounds based on the range of grain sizes for each sample. The resulting calculated grain sizes for each phase angle are shown in Table 5. In the case of enstatite, the best fit is achieved when both the small and medium grain size samples calculated to have similar mean grain sizes of ~63 μm. The calculated grain size for the smalles grain size sample pins at the top of the grain size range (63 μm), regardless of phase angle. This may be due to over-processing of the sample, where too much of the smaller grains were removed during the fines removal process, skewing the overall grain size to higher than expected. However, there are other explanations. Grain size is one of the largest contributing factors to overall reflectance (Helfenstein & Shepard, 2011). If some other phenomena were darkening the spectrum, the model would likely use grain size to reflect that change. This could include small dark inclusions, admixing of the sample cup from sample of insufficient depth or spot size, among others. In the end, it is important to remember that this parameter is related to grain size but is mathematically the average path length traveled by the light before being scattered, reflected, or absorbed. The large grain size of enstatite fits well within the expected range with a minimal variation with phase angle (Table 5). In the case of ferroenstatite, there is a clear relationship between larger overall *k* values and lower grain size estimates, however there is not a deviation of overall reflectance with phase angle that could account for this behavior. Ultimately, the model should arrive at a single grain size value regardless of phase angle, but this relationship between larger grain size estimates and lower reflectance values is likely influenced by the isotropic nature of the Spectralon as well as other phenomena not explicitly modeled here, such as microscopic surface roughness or shadow hiding. An in-depth study of the effect of grain size, grain shape, sample packing, and sample composition is beyond the scope of this paper but would shed light on these modeling results.

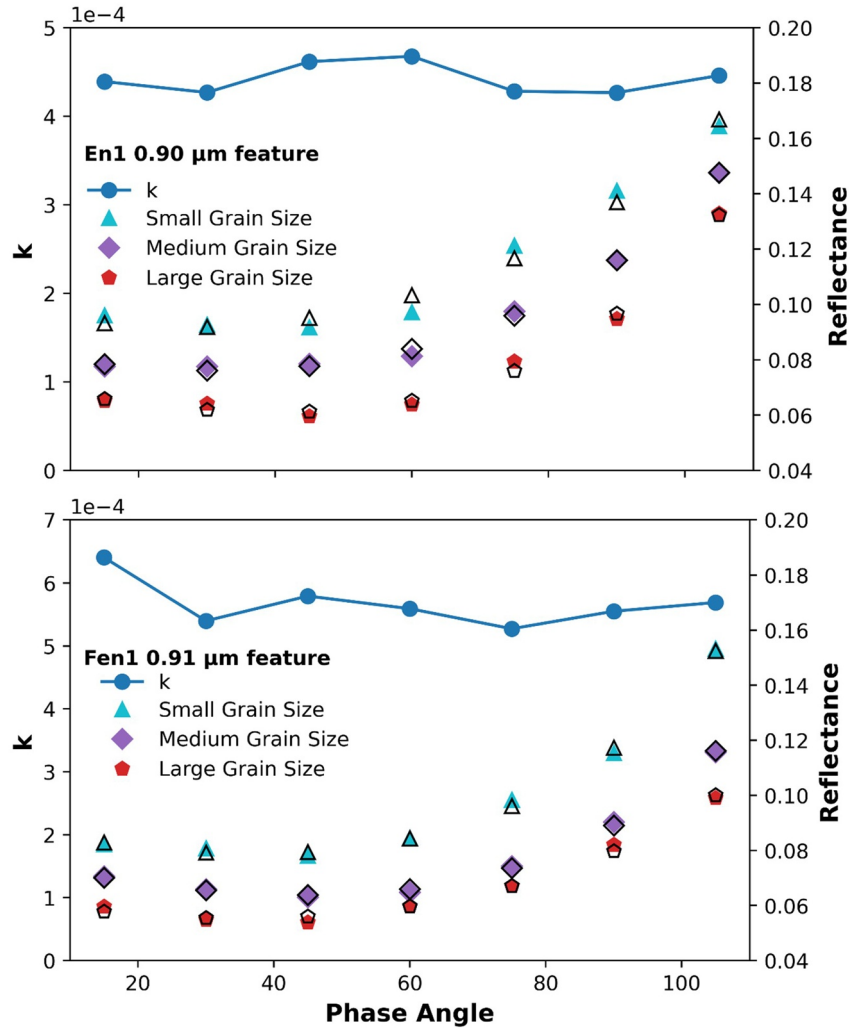

Figure 12. Maximum k value (filled circles) at the ~0.9 µm with phase angle for enstatite (top) and ferroenstatite (bottom). Maximum reflectance value for the small grain size (triangles), medium grain sizes (diamonds) and large grain size (pentagon) at the ~0.9 µm for enstatite (top) and ferroenstatite (bottom). Filled reflectance symbols represent measured reflectance, and hollow black symbols represent the modeled value.

Another contribution to model errors we must consider in our approach is the porosity correction. As discussed by Sklute et al. (2015), there is a large degree of uncertainty with its value if accounted for in the model. For this reason, we report *n* and *k* with an uncorrected porosity factor. However, this can result in the *k* values being too

Table 5
Calculated Grain Size

Sample	Actual grain size range (µm)	$g = 15°$	$g = 30°$	$g = 45°$	$g = 60°$	$g = 75°$	$g = 90°$	$g = 105°$
Enstatite	45–63	63.00	63.00	63.00	63.00	63.00	63.00	63.00
	63–90	60.90	65.47	60.37	62.94	61.92	63.55	63.03
	90–120	101.93	95.27	96.38	95.17	98.25	104.72	96.52
Ferroenstatite	45–63	41.06	53.87	44.74	52.94	54.24	52.14	51.21
	63–90	70.73	90.00	72.06	90.00	90.00	90.00	84.73
	90–120	80.56	107.85	88.86	102.22	103.50	109.07	99.56

Note. *g* is the phase angle.

small by up to a factor of 2 (Hapke, 2002). Using the raw data provided with this paper along with the computer program available as part of this work, the interested reader is able to explore the interaction between n, k, and porosity. The optical constants presented here were calculated using a set of assumptions common in the literature (e.g., Roush et al., 1991). Decreasing the number of assumptions necessarily increases the number of modeling parameters, thus affecting the uniqueness of the solution. The methodology used in this paper seeks to strike a balance between limiting assumptions and uniqueness of fit while providing the tools and data for further exploration.

6. Conclusions

We have provided a comprehensive data set of optical constants of two compositions of natural OPX for use by the Earth and planetary remote sensing communities. This study focused on two distinct compositions and, while other studies have concentrated on the NIR with synthetic ortho- and clino- pyroxenes across a wide range of compositions (Denevi et al., 2007; Lucey, 1998; Trang et al., 2013), there is still a lack of oriented optical constant data in the MIR for more iron-rich orthopyroxene species. This is mostly due to the lack of natural or synthetic single crystals of Fe-rich OPX large enough for current benchtop analytical capabilities. With the detection of Fe-rich OPX in eucritic meteorites (Pang et al., 2016), it is possible this mineral species may be an important component on other differentiated asteroids. Thus, future work widening the available orthopyroxene data set to include oriented MIR data for Fe-rich compositions will aid in these studies. Additionally, the anomalous behavior observed here in the variation of VNIR k with phase angle at the absorption maxima could not be completely explained as no systematic effects of the modeled reflectance or grain size estimates could be directly correlated with the observed behavior. While tracking the source of this discrepancy is outside of the scope of the current work, future work should be conducted to explain these aspects of Hapke theory. The updated Sklute et al., 2021 Matlab code is available for download at https://zenodo.org/record/4429127.

Data Availability Statement

Data presented here are permanently archived at Zenodo.org at doi:10.5281/zenodo.4758045.

Acknowledgments
The authors would like to thank Dr. Xianyin Chen and Dr. Anna Plonka for their help with orienting the single crystal samples, Reed Hopkins for his help acquiring powder X-ray diffraction of the powdered samples, and Katlyn Lafranca for her indispensable help in the preparation of the grain size fractions used in this study. Support for this work was provided by NSF CAREER award 1150652 to T. D. Glotch and the RIS^{4}E and RISE2 nodes of NASA's Solar System Exploration Research Virtual Institute (awards NNA14AB04A and 80NSSC19M0215 to T. D. Glotch).

References

Adams, J. B. (1974). Visible and near-infrared diffuse reflectance spectra of pyroxenes as applied to remote sensing of solid objects in the solar system. *Journal of Geophysical Research*, *79*(32), 4829–4836. https://doi.org/10.1029/JB079i032p04829

Anovitz, L. M., Essene, E. J., & Dunham, W. R. (1988). Order-disorder experiments on orthopyroxenes; implications for the orthopyroxene geospeedometer. *American Mineralogist*, *73*(9–10), 1060–1073.

Arnold, J. A., Glotch, T. D., Lucey, P. G., Song, E., Thomas, I. R., Bowles, N. E., & Greenhagen, B. T. (2016). Constraints on olivine-rich rock types on the Moon as observed by Diviner and M ^{3}: Implications for the formation of the lunar crust: Constraints on olivine-rich rock types on the moon. *Journal of Geophysical Research: Planets*, *121*(7), 1342–1361. https://doi.org/10.1002/2015JE004874

Arnold, J. A., Glotch, T. D., & Plonka, A. M. (2014). Mid-infrared optical constants of clinopyroxene and orthoclase derived from oriented single-crystal reflectance spectra. *American Mineralogist*, *99*(10), 1942–1955. https://doi.org/10.2138/am-2014-4828

Aronson, J. R. (1986). Optical constants of monoclinic anisotropic crystals: Orthoclase. *Spectrochimica Acta Part A: Molecular Spectroscopy*, *42*(2–3), 187–190. https://doi.org/10.1016/0584-8539(86)80178-7

Aronson, J. R., Emslie, A. G., Miseo, E. V., Smith, E. M., & Strong, P. F. (1983). Optical constants of monoclinic anisotropic crystals: Gypsum. *Applied Optics*, *22*(24), 4093. https://doi.org/10.1364/AO.22.004093

Bandfield, J. L. (2000). A global view of Martian surface compositions from MGS-TES. *Science*, *287*(5458), 1626–1630. https://doi.org/10.1126/science.287.5458.1626

Bibring, J.-P. (2005). Mars surface diversity as revealed by the OMEGA/Mars express observations. *Science*, *307*(5715), 1576–1581. https://doi.org/10.1126/science.1108806

Bibring, J.-P., Langevin, Y., Mustard, J. F., Poulet, F., Arvidson, R., Gendrin, A., et al. (2006). Global mineralogical and aqueous Mars history derived from OMEGA/Mars express data. *Science*, *312*(5772), 400–404. https://doi.org/10.1126/science.1122659

Bouwman, J., Meeus, G., deKoter, A., Hony, S., Dominik, C., & Waters, L. B. F. M. (2001). Processing of silicate dust grains in Herbig Ae/Be systems. *Astronomy & Astrophysics*, *375*(3), 950–962. https://doi.org/10.1051/0004-6361:20010878

Bradley, J. P., Brownlee, D. E., & Veblen, D. R. (1983). Pyroxene whiskers and platelets in interplanetary dust: Evidence of vapour phase growth. *Nature*, *301*(5900), 473–477. https://doi.org/10.1038/301473a0

Burns, R. G. (1965). *Electronic spectra of silicate minerals: Application of crystal-field theory to aspects of geochemistry* [Ph.D Thesis]. University of California..

Cahill, J. T., & Lucey, P. G. (2007). Radiative transfer modeling of lunar highlands spectral classes and relationship to lunar samples. *Journal of Geophysical Research*, *112*(E10), E10007. https://doi.org/10.1029/2006JE002868

Cahill, J. T. S., Lucey, P. G., & Wieczorek, M. A. (2009). Compositional variations of the lunar crust: Results from radiative transfer modeling of central peak spectra. *Journal of Geophysical Research*, *114*(E9), E09001. https://doi.org/10.1029/2008JE003282

Cameron, M., & Papike, J. J. (1981). Structural and chemical variations in proxenes. *American Mineralogist*, *66*, 1–50.

Chandrasekhar, S. (1960). *Radiative transfer*. Dover Publications.

Chapman, C. R., Morrison, D., & Zellner, B. (1975). Surface properties of asteroids: A synthesis of polarimetry, radiometry, and spectrophotometry. *Icarus*, *25*(1), 104–130. https://doi.org/10.1016/0019-1035(75)90191-8

Chihara, H., Koike, C., Tsuchiyama, A., Tachibana, S., & Sakamoto, D. (2002). Compositional dependence of infrared absorption spectra of crystalline silicates: I. Mg–Fe pyroxenes. *Astronomy & Astrophysics*, *391*(1), 267–273. https://doi.org/10.1051/0004-6361:20020791

Cloutis, E. A., & Gaffey, M. J. (1991a). Pyroxene spectroscopy revisited: Spectral-compositional correlations and relationship to geothermometry. *Journal of Geophysical Research*, *96*(E5), 22809. https://doi.org/10.1029/91JE02512

Cloutis, E. A., & Gaffey, M. J. (1991b). Spectral-compositional variations in the constituent minerals of mafic and ultramafic assemblages and remote sensing implications. *Earth, Moon, and Planets*, *53*(1), 11–53. https://doi.org/10.1007/bf00116217

Conel, J. E. (1969). Infrared emissivities of silicates: Experimental results and a cloudy atmosphere model of Spectral emission from condensed particulate mediums. *Journal of Geophysical Research*, *74*(6), 1614–1634. https://doi.org/10.1029/JB074i006p01614

DellaGiustina, D. N., Kaplan, H. H., Simon, A. A., Bottke, W. F., Avdellidou, C., Delbo, M., et al. (2021). Exogenic basalt on asteroid (101955) Bennu. *Nature Astronomy*, *5*(1), 31–38. https://doi.org/10.1038/s41550-020-1195-z

Demichelis, R., Suto, H., Noël, Y., Sogawa, H., Naoi, T., Koike, C., et al. (2012). The infrared spectrum of ortho-enstatite from reflectance experiments and first-principle simulations: The IR spectrum of ortho-enstatite. *Monthly Notices of the Royal Astronomical Society*, *420*(1), 147–154. https://doi.org/10.1111/j.1365-2966.2011.20018.x

Denevi, B. W., Lucey, P. G., Hochberg, E. J., & Steutel, D. (2007). Near-infrared optical constants of pyroxene as a function of iron and calcium content. *Journal of Geophysical Research*, *112*(E5), E05009. https://doi.org/10.1029/2006JE002802

De Sanctis, M. C., Ammannito, E., Capria, M. T., Tosi, F., Capaccioni, F., Zambon, F., et al. (2012). Spectroscopic characterization of mineralogy and its diversity across Vesta. *Science*, *336*(6082), 697–700. https://doi.org/10.1126/science.1219270

Donaldson Hanna, K. L., Thomas, I. R., Bowles, N. E., Greenhagen, B. T., Pieters, C. M., Mustard, J. F., et al. (2012). Laboratory emissivity measurements of the plagioclase solid solution series under varying environmental conditions: Spectral measurements of plagioclase. *Journal of Geophysical Research*, *117*(E11), E11004. https://doi.org/10.1029/2012JE004184

Dorschner, J., Begemann, B., Henning, T., Jaeger, C., & Mutschke, H. (1995). Steps toward interstellar silicate mineralogy. II. Study of Mg-Fe-silicate glasses of variable composition. *Astronomy and Astrophysics*, *300*, 503.

Drake, M. J. (1979). Geochemical evolution of the eucrite parent body: Possible nature and evolution of asteroid 4 Vesta. In *Asteroids and planets X* (pp. 765–782). University of Atizona Press..

Dyar, M. D., Sklute, E. C., Menzies, O. N., Bland, P. A., Lindsley, D., Glotch, T. D., et al. (2009). Spectroscopic characteristics of synthetic olivine: An integrated multi-wavelength and multi-technique approach. *American Mineralogist*, *94*(7), 883–898. https://doi.org/10.2138/am.2009.3115

Ehlmann, B. L., Klima, R. L., Bennett, C. L., Blaney, D., Bowles, N. E., Calcutt, S., et al. (2021). Lunar trailblazer: A pioneering smallsat for lunar water and lunar geology. In *52nd lunar and planetary science conference 2021*.

Farmer, V. C. (Ed.), (1974). *The infrared spectra of minerals* (Vol. 4). Mineralogical Society of Great Britain and Ireland. https://doi.org/10.1180/mono-4

Feierberg, M. A., & Drake, M. J. (1980). The meteorite-asteroid connection: The infrared spectra of Eucrites, Shergottites, and Vesta. *Science*, *209*(4458), 805–807. https://doi.org/10.1126/science.209.4458.805

Gaffey, M. J. (1997). Surface lithologic heterogeneity of asteroid 4 Vesta. *Icarus*, *127*(1), 130–157. https://doi.org/10.1006/icar.1997.5680

Gaffey, M. J., Bell, J. F., Brown, R. H., Burbine, T. H., Piatek, J. L., Reed, K. L., & Chaky, D. A. (1993). Mineralogical variations within the S-type Asteroid class. *Icarus*, *106*(2), 573–602. https://doi.org/10.1006/icar.1993.1194

Gaffey, M. J., & McCord, T. B. (1978). Asteroid surface materials: Mineralogical characterizations from reflectance spectra. *Space Science Reviews*, *21*(5), 555–628. https://doi.org/10.1007/bf00240908

Glotch, T. D., Bandfield, J. L., Lucey, P. G., Hayne, P., Greenhagen, B. T., Arnold, J. A., et al. (2015). Formation of lunar swirls by magnetic field standoff of the solar wind. *Nature Communications*, *6*(1), 6189. https://doi.org/10.1038/ncomms7189

Glotch, T. D., Christensen, P. R., & Sharp, T. G. (2006). Fresnel modeling of hematite crystal surfaces and application to martian hematite spherules. *Icarus*, *181*(2), 408–418. https://doi.org/10.1016/j.icarus.2005.11.020

Glotch, T. D., Hagerty, J. J., Lucey, P. G., Hawke, B. R., Giguere, T. A., Arnold, J. A., et al. (2011). The mairan domes: Silicic volcanic constructs on the moon: The silicic mairan domes. *Geophysical Research Letters*, *38*(21), L21204. https://doi.org/10.1029/2011GL049548

Glotch, T. D., Lucey, P. G., Bandfield, J. L., Greenhagen, B. T., Thomas, I. R., Elphic, R. C., et al. (2010). Highly silicic compositions on the moon. *Science*, *329*(5998), 1510–1513. https://doi.org/10.1126/science.1192148

Glotch, T. D., & Rossman, G. R. (2009). Mid-infrared reflectance spectra and optical constants of six iron oxide/oxyhydroxide phases. *Icarus*, *204*(2), 663–671. https://doi.org/10.1016/j.icarus.2009.07.024

Glotch, T. D., Rossman, G. R., & Aharonson, O. (2007). Mid-infrared (5–100 μm) reflectance spectra and optical constants of ten phyllosilicate minerals. *Icarus*, *192*(2), 605–622. https://doi.org/10.1016/j.icarus.2007.07.002

Greenhagen, B. T., Lucey, P. G., Wyatt, M. B., Glotch, T. D., Allen, C. C., Arnold, J. A., et al. (2010). Global silicate mineralogy of the moon from the diviner lunar radiometer. *Science*, *329*(5998), 1507–1509. https://doi.org/10.1126/science.1192196

Hamilton, V. E. (2000). Thermal infrared emission spectroscopy of the pyroxene mineral series. *Journal of Geophysical Research*, *105*(E4), 9701–9716. https://doi.org/10.1029/1999JE001112

Hanner, M. S., Lynch, D. K., & Russell, R. W. (1994). The 8-13 micron spectra of comets and the composition of silicate grains. *The Astrophysical Journal*, *425*, 274–285. https://doi.org/10.1086/173984

Hapke, B. (1981). Bidirectional reflectance spectroscopy: 1. Theory. *Journal of Geophysical Research*, *86*(B4), 3039–3054. https://doi.org/10.1029/JB086iB04p03039

Hapke, B. (1996). A model of radiative and conductive energy transfer in planetary regoliths. *Journal of Geophysical Research*, *101*(E7), 16817–16831. https://doi.org/10.1029/96JE00917

Hapke, B. (2002). Bidirectional reflectance spectroscopy. *Icarus*, *157*(2), 523–534. https://doi.org/10.1006/icar.2002.6853

Hapke, B. (2012). *Theory of reflectance and emittance spectroscopy* (2nd ed.). Cambridge University Press.

Hardersen, P. S., Gaffey, M. J., & Abell, P. A. (2005). Near-IR spectral evidence for the presence of iron-poor orthopyroxenes on the surfaces of six M-type asteroids. *Icarus*, *175*(1), 141–158. https://doi.org/10.1016/j.icarus.2004.10.017

Helfenstein, P., & Shepard, M. K. (2011). Testing the Hapke photometric model: Improved inversion and the porosity correction. *Icarus*, *215*(1), 83–100. https://doi.org/10.1016/j.icarus.2011.07.002

Henning, T., & Mutschke, H. (1997). Low-temperature infrared properties of cosmic dust analogues. *Astronomy & Astrophysics*, *327*, 743–754.

Jäger, C., Molster, F. J., Dorschner, J., Mutschke, H., & Waters, L. B. F. M. (1998). Steps toward interstellar silicate mineralogy. IV. The crystalline revolution. *Astronomy & Astrophysics*, *339*, 904–916.

Jäger, C., Mutschke, H., Begemann, B., Dorschner, J., & Henning, T. (1994). Steps toward interstellar silicate mineralogy. 1: Laboratory results of a silicate glass of mean cosmic composition. *Astronomy & Astrophysics*, *292*, 641–655.

Klima, R. L., Dyar, M. D., & Pieters, C. M. (2011a). Near-infrared spectra of clinopyroxenes: Effects of calcium content and crystal structure: Near-infrared spectra of clinopyroxenes. *Meteoritics & Planetary Sciences*, *46*(3), 379–395. https://doi.org/10.1111/j.1945-5100.2010.01158.x

Klima, R. L., Pieters, C. M., Boardman, J. W., Green, R. O., Head, J. W., Isaacson, P. J., et al. (2011b). New insights into lunar petrology: Distribution and composition of prominent low-Ca pyroxene exposures as observed by the Moon Mineralogy Mapper (M ^{3}). *Journal of Geophysical Research*, *116*, E00G06. https://doi.org/10.1029/2010JE003719

Klima, R. L., Pieters, C. M., & Dyar, M. D. (2007). Spectroscopy of synthetic Mg-Fe pyroxenes I: Spin-allowed and spin-forbidden crystal field bands in the visible and near-infrared. *Meteoritics & Planetary Sciences*, *42*(2), 235–253. https://doi.org/10.1111/j.1945-5100.2007.tb00230.x

Klima, R. L., Pieters, C. M., & Dyar, M. D. (2008). Characterization of the 1.2 μm M1 pyroxene band: Extracting cooling history from near-IR spectra of pyroxenes and pyroxene-dominated rocks. *Meteoritics & Planetary Sciences*, *43*(10), 1591–1604. https://doi.org/10.1111/j.1945-5100.2008.tb00631.x

Koike, C., Tsuchiyama, A., Shibai, H., Suto, H., Chihara, H., Sogawa, H., et al. (2000). Absorption spectra of Mg-rich Mg-Fe and Ca pyroxenes in the mid-and far-infrared regions. *Astronomy & Astrophysics*, *363*, 1115–1122.

Lane, M. D. (1999). Midinfrared optical constants of calcite and their relationship to particle size effects in thermal emission spectra of granular calcite. *Journal of Geophysical Research*, *104*(E6), 14099–14108. https://doi.org/10.1029/1999JE900025

Lindsley, D. H. (1983). Pyroxene thermometry. *American Mineralogist*, *68*(5–6), 477–493.

Lucey, P. G. (1998). Model near-infrared optical constants of olivine and pyroxene as a function of iron content. *Journal of Geophysical Research*, *103*(E1), 1703–1713. https://doi.org/10.1029/97JE03145

Lucey, P. G., Greenhagen, B., Donaldson Hanna, K., Bowles, N., Flom, A., & Paige, D. A. (2021). Christiansen feature map from the lunar reconnaissance orbiter diviner lunar radiometer experiment: Improved corrections and derived mineralogy. *Journal of Geophysical Research: Planets*, *126*(6), e2020JE006777. https://doi.org/10.1029/2020JE006777

Lumme, K., & Bowell, E. (1981). Radiative transfer in the surfaces of atmosphereless bodies. I-Theory. II-Interpretation of phase curves. *The Astronomical Journal*, *86*, 1694–1721. https://doi.org/10.1086/113054

Mackinnon, I. D. R., & Rietmeijer, F. J. M. (1987). Mineralogy of chondritic interplanetary dust particles. *Reviews of Geophysics*, *25*(7), 1527. https://doi.org/10.1029/RG025i007p01527

Malfait, K., Waelkens, C., Waters, L. B. F. M., Vandenbussche, B., Huygen, E., & deGraauw, M. S. (1998). The spectrum of the young star HD 100546 observed with the Infrared Space Observatory. *Astronomy & Astrophysics*, *332*, L25–L28.

McCord, T. B., Adams, J. B., & Johnson, T. V. (1970). Asteroid Vesta: Spectral reflectivity and compositional implications. *Science*, *168*(3938), 1445–1447. https://doi.org/10.1126/science.168.3938.1445

Mishchenko, M. I., Dlugach, J. M., Yanovitskij, E. G., & Zakharova, N. T. (1999). Bidirectional reflectance of flat, optically thick particulate layers: An efficient radiative transfer solution and applications to snow and soil surfaces. *Journal of Quantitative Spectroscopy and Radiative Transfer*, *63*(2–6), 409–432. https://doi.org/10.1016/S0022-4073(99)00028-X

Molina, G., & Zanazzi, P. F. (1991). Intracrystalline Fe2+ -Mg ordering in augite: Experimental study and geothermometric applications. *European Journal of Mineralogy*, *3*(5), 863–876. https://doi.org/10.1127/ejm/3/5/0863

Molster, F. J., Waters, L. B. F. M., Tielens, A. G. G. M., & Barlow, M. J. (2002). Crystalline silicate dust around evolved stars: I. The sample stars. *Astronomy & Astrophysics*, *382*(1), 184–221. https://doi.org/10.1051/0004-6361:20011550

Morimoto, N., Fabries, J., Furguson, A. K., Ginzburg, I. V., Ross, M., Seifert, F. A., et al. (1988). Nomenclature of pyroxenes. *American Mineralogist*, *73*, 1123–1133. https://doi.org/10.1180/minmag.1988.052.367.15

Mustard, J. F., Murchie, S., Erard, S., & Sunshine, J. (1997). In situ compositions of Martian volcanics: Implications for the mantle. *Journal of Geophysical Research*, *102*(E11), 25605–25615. https://doi.org/10.1029/97JE02354

Nash, D. B., Salisbury, J. W., Conel, J. E., Lucey, P. G., & Christensen, P. R. (1993). Evaluation of infrared emission spectroscopy for mapping the moon's surface composition from lunar orbit. *Journal of Geophysical Research*, *98*(E12), 23535–23552. https://doi.org/10.1029/93JE02604

Pang, R.-L., Zhang, A.-C., Wang, S.-Z., Wang, R.-C., & Yurimoto, H. (2016). High-pressure minerals in eucrite suggest a small source crater on Vesta. *Scientific Reports*, *6*(1), 26063. https://doi.org/10.1038/srep26063

Papike, J. J., Karner, J. M., Shearer, C. K., & Burger, P. V. (2009). Silicate mineralogy of martian meteorites. *Geochimica et Cosmochimica Acta*, *73*(24), 7443–7485. https://doi.org/10.1016/j.gca.2009.09.008

Piatek, J. L. (2003). *Size-dependent scattering properties of planetary regolith analogs* [Ph.D Thesis]. University of Pittsburgh.

Rogers, A. D., Bandfield, J. L., & Christensen, P. R. (2007). Global spectral classification of Martian low-albedo regions with Mars global surveyor thermal emission spectrometer (MGS-TES) data. *Journal of Geophysical Research*, *112*(E2), E02004. https://doi.org/10.1029/2006JE002726

Rogers, A. D., & Christensen, P. R. (2007). Surface mineralogy of Martian low-albedo regions from MGS-TES data: Implications for upper crustal evolution and surface alteration. *Journal of Geophysical Research*, *112*(E1), E01003. https://doi.org/10.1029/2006JE002727

Rossman, G. R. (1980). Pyroxene spectroscopy. In *Pyroxenes. Reviews in mineralogy* (Vol. 7, pp. 93–115). Mineralogical Society of America. https://doi.org/10.1515/9781501508257-007

Roush, T. (2021). Estimation of visible, near- and mid-infrared complex refractive indices of calcite, dolomite, and magnesite. *Icarus*, *354*, 114056. https://doi.org/10.1016/j.icarus.2020.114056

Roush, T., Pollack, J., & Orenberg, J. (1991). Derivation of midinfrared (5–25 μm) optical constants of some silicates and palagonite. *Icarus*, *94*(1), 191–208. https://doi.org/10.1016/0019-1035(91)90150-R

Salisbury, J. W. (1972). Spectroscopic remote sensing of lunar surface composition. *The Moon*, *5*(3–4), 332–347. https://doi.org/10.1007/BF00563087

Salisbury, J. W., & Wald, A. (1992). The role of volume scattering in reducing spectral contrast of reststrahlen bands in spectra of powdered minerals. *Icarus*, *96*(1), 121–128. https://doi.org/10.1016/0019-1035(92)90009-V

Salisbury, J. W., & Walter, L. S. (1989). Thermal infrared (2.5–13.5 μm) spectroscopic remote sensing of igneous rock types on particulate planetary surfaces. *Journal of Geophysical Research*, *94*(B7), 9192–9202. https://doi.org/10.1029/JB094iB07p09192

Sandford, S. A., & Walker, R. M. (1985). Laboratory infrared transmission spectra of individual interplanetary dust particles from 2.5 to 25 microns. *The Astrophysical Journal*, *291*, 838–851. https://doi.org/10.1086/163120

Saxena, S. K., Ghose, S., & Turnock, A. C. (1974). Cation distribution in low-calcium pyroxenes: Dependence on temperature and calcium content and the thermal history of lunar and terrestrial pigeonites. *Earth and Planetary Science Letters*, *21*(2), 194–200. https://doi.org/10.1016/0012-821X(74)90054-5

Shkuratov, Y., Starukhina, L., Hoffmann, H., & Arnold, G. (1999). A model of spectral albedo of particulate surfaces: Implications for optical properties of the moon. *Icarus*, *137*(2), 235–246. https://doi.org/10.1006/icar.1998.6035

Sklute, E. C., Domingue-Loren, D., Glotch, T. D., Rucks, M., & Ye, C. (2021). *A new open-source hapke radiative transfer program for determining optical constants and analyzing phase behavior*. LPSC.

Sklute, E. C., Glotch, T. D., Piatek, J. L., Woerner, W. R., Martone, A. A., & Kraner, M. L. (2015). Optical constants of synthetic potassium, sodium, and hydronium jarosite. *American Mineralogist*, *100*(5–6), 1110–1122. https://doi.org/10.2138/am-2015-4824

Song, E., Bandfield, J. L., Lucey, P. G., Greenhagen, B. T., & Paige, D. A. (2013). Bulk mineralogy of lunar crater central peaks via thermal infrared spectra from the diviner lunar radiometer: A study of the Moon's crustal composition at depth: Mineralogy of lunar crater central peaks. *Journal of Geophysical Research: Planets*, *118*(4), 689–707. https://doi.org/10.1002/jgre.20065

Spitzer, W. G., & Kleinman, D. A. (1961). Infrared lattice bands of quartz. *Physical Review*, *121*(5), 1324–1335. https://doi.org/10.1103/PhysRev.121.1324

Sunshine, J. M., Bus, S. J., McCoy, T. J., Burbine, T. H., Corrigan, C. M., & Binzel, R. P. (2004). High-calcium pyroxene as an indicator of igneous differentiation in asteroids and meteorites. *Meteoritics & Planetary Sciences*, *39*(8), 1343–1357. https://doi.org/10.1111/j.1945-5100.2004.tb00950.x

Sunshine, J. M., & Pieters, C. M. (1993). Estimating modal abundances from the spectra of natural and laboratory pyroxene mixtures using the modified Gaussian model. *Journal of Geophysical Research*, *98*(E5), 9075–9087. https://doi.org/10.1029/93JE00677

Sunshine, J. M., Pieters, C. M., & Pratt, S. F. (1990). Deconvolution of mineral absorption bands: An improved approach. *Journal of Geophysical Research*, *95*(B5), 6955–6966. https://doi.org/10.1029/JB095iB05p06955

Suto, H., Koike, C., Sogawa, H., Tsuchiyama, A., Chihara, H., & Mizutani, K. (2002). Infrared spectra of fayalite crystal. *Astronomy & Astrophysics*, *389*(2), 568–571. https://doi.org/10.1051/0004-6361:20020501

Tompkins, S., & Pieters, C. M. (1999). Mineralogy of the lunar crust: Results from clementine. *Meteoritics & Planetary Sciences*, *34*(1), 25–41. https://doi.org/10.1111/j.1945-5100.1999.tb01729.x

Trang, D., Lucey, P. G., Gillis-Davis, J. J., Cahill, J. T. S., Klima, R. L., & Isaacson, P. J. (2013). Near-infrared optical constants of naturally occurring olivine and synthetic pyroxene as a function of mineral composition: Olivine and pyroxene optical constants. *Journal of Geophysical Research: Planets*, *118*(4), 708–732. https://doi.org/10.1002/jgre.20072

Virgo, D., & Hafner, S. S. (1970). Fe2+,Mg order-disorder in natural orthopyroxenes. *American Mineralogist*, *55*(1–2), 201–223.

Waters, L. B. F. M., Beintema, D. A., Zijlstra, A. A., deKoter, A., Molster, F. J., Bouwman, J., et al. (1998). Crystalline silicates in Planetary Nebulae with [WC] central stars. *Astronomy & Astrophysics, Letters*, *331*, L61.

Wenrich, M. L., & Christensen, P. R. (1996). Optical constants of minerals derived from emission spectroscopy: Application to quartz. *Journal of Geophysical Research*, *101*(B7), 15921–15931. https://doi.org/10.1029/96JB01153

Yang, Y., Li, S., Milliken, R. E., Zhang, H., Robertson, K., & Hiroi, T. (2019). Phase functions of typical lunar surface minerals derived for the Hapke model and implications for visible to near-infrared (VNIR) spectral unmixing. *Journal of Geophysical Research: Planets*, *124*, 31–60. https://doi.org/10.1029/2018JE005713

Ye, C., Rucks, M. J., Arnold, J. A., & Glotch, T. D. (2019). Mid-infrared optical constants of labradorite, a triclinic plagioclase mineral. *Earth and Space Science*, *6*(12), 2410–2422. https://doi.org/10.1029/2019EA000915

Ye, C., Sklute, E. C., & Glotch, T. D. (2021). Orientation averaged visible/near-infrared and mid-infrared optical constants of hydrous Ca-sulfates: Gypsum and bassanite. *Earth and Space Science*, *8*, e01834.

Zeidler, S., Mutschke, H., & Posch, T. (2015). Temperature-dependent infrared optical constants of olivine and enstatite. *The Astrophysical Journal*, *798*(2), 125. https://doi.org/10.1088/0004-637X/798/2/125